Article

Structural insights into the high-affinity IgE receptor FcεRI complex

https://doi.org/10.1038/s41586-024-07864-5

Received: 12 February 2024

Accepted: 22 July 2024

Published online: 21 August 2024

Check for updates

Meijie Deng[1,5], Shuo Du[2,5]✉, Handi Hou[2,3] & Junyu Xiao[1,2,3,4]✉

Immunoglobulin E (IgE) plays a pivotal role in allergic responses[1,2]. The high-affinity IgE receptor, FcεRI, found on mast cells and basophils, is central to the effector functions of IgE. FcεRI is a tetrameric complex, comprising FcεRIα, FcεRIβ and a homodimer of FcRγ (originally known as FcεRIγ), with FcεRIα recognizing the Fc region of IgE (Fcε) and FcεRIβ–FcRγ facilitating signal transduction[3]. Additionally, FcRγ is a crucial component of other immunoglobulin receptors, including those for IgG (FcγRI and FcγRIIIA) and IgA (FcαRI)[4–8]. However, the molecular basis of FcεRI assembly and the structure of FcRγ have remained elusive. Here we elucidate the cryogenic electron microscopy structure of the Fcε–FcεRI complex. FcεRIα has an essential role in the receptor's assembly, interacting with FcεRIβ and both FcRγ subunits. FcεRIβ is structured as a compact four-helix bundle, similar to the B cell antigen CD20. The FcRγ dimer exhibits an asymmetric architecture, and coils with the transmembrane region of FcεRIα to form a three-helix bundle. A cholesterol-like molecule enhances the interaction between FcεRIβ and the FcεRIα–FcRγ complex. Our mutagenesis analyses further indicate similarities between the interaction of FcRγ with FcεRIα and FcγRIIIA, but differences in that with FcαRI. These findings deepen our understanding of the signalling mechanisms of FcεRI and offer insights into the functionality of other immune receptors dependent on FcRγ.

Immunoglobulins, also known as antibodies, play a crucial role in the immune system by recognizing and neutralizing harmful substances. They exert their function by binding to specific Fc receptors, which in turn trigger immune responses[6,7]. There are five classes of human immunoglobulin (IgA, IgD, IgE, IgG and IgM), each characterized by a unique Fc region that is recognized by corresponding Fc receptors[9]. Among these, IgE is notable for its role in defending against parasitic infections and also its involvement in allergic reactions. Consequently, it has become a focal point for the development of anti-allergic medications[1,2]. The high-affinity IgE Fc receptor, FcεRI, is intimately linked to IgE-mediated allergic diseases.

On mast cells and basophils, which are pivotal in cellular degranulation and allergic responses, FcεRI is present as a tetramer composed of one FcεRIα chain, one FcεRIβ chain and two FcRγ (also known as FcεRIγ) chains[10,11]. The FcεRIα chain includes an extracellular domain (sFcεRIα) that binds to Fcε, a single transmembrane (TM) helix and a short cytoplasmic tail. The removal of the cytoplasmic tail of FcεRIα does not impair the receptor's function, indicating that its primary role is to recognize IgE, whereas the FcεRIβ and FcRγ chains are responsible for signal transduction[12]. FcεRIβ is a member of the membrane-spanning 4A (MS4A) family and contains an intracellular immunoreceptor tyrosine-based activation motif (ITAM), which is phosphorylated by Src family kinases, particularly Lyn, to initiate or enhance IgE signalling pathways[3,13]. Similarly, FcRγ is equipped with an ITAM motif and acts as a signalling adaptor in the FcεRI complex[14]. In humans, FcεRI also exists in other cell types, including antigen-presenting cells, as an αγ2 trimer that lacks the FcεRIβ chain[15]. Despite its importance, the underlying molecular mechanism of the FcεRI assembly has remained incompletely understood.

Originally identified as the third component of the FcεRI complex (hence the name FcεRIγ), the FcRγ chain has since been recognized as an integral part of several other Fc receptors. These include FcγRI (also known as CD64) and FcγRIIIA (also known as CD16A), which bind to IgG, as well as FcαRI (also known as CD89), the receptor for IgA. Consequently, it is now more widely known as the Fc receptor gamma chain (FcRγ)[8]. The binding of specific antibody–antigen complexes to their corresponding receptors triggers the phosphorylation of the ITAM motif on FcRγ, which then recruits and activates the spleen tyrosine kinase, initiating a cascade of effector functions[7,16,17]. Beyond these roles, FcRγ is also associated with a variety of other immunoreceptors, especially the leukocyte receptor cluster (LRC) family members, such as the natural cytotoxicity triggering receptor 1 (NCR1; also known as NKp46), the platelet collagen receptor glycoprotein VI (GPVI) and the osteoclast-associated receptor (OSCAR), among others[4,5]. Furthermore, the TM region of FcRγ shares notable homology with that of CD3ζ (CD247), which is an essential part of the T cell receptor (TCR) complex[18]. Nevertheless, the precise molecular mechanisms underlying the function of FcRγ remain to be fully elucidated.

[1]State Key Laboratory of Protein and Plant Gene Research, School of Life Sciences, Peking University, Beijing, People's Republic of China. [2]Changping Laboratory, Beijing, People's Republic of China. [3]Academy for Advanced Interdisciplinary Studies, Peking University, Beijing, People's Republic of China. [4]Peking-Tsinghua Center for Life Sciences, Peking University, Beijing, People's Republic of China. [5]These authors contributed equally: Meijie Deng, Shuo Du. ✉e-mail: a0000426@cpl.ac.cn; junyuxiao@pku.edu.cn

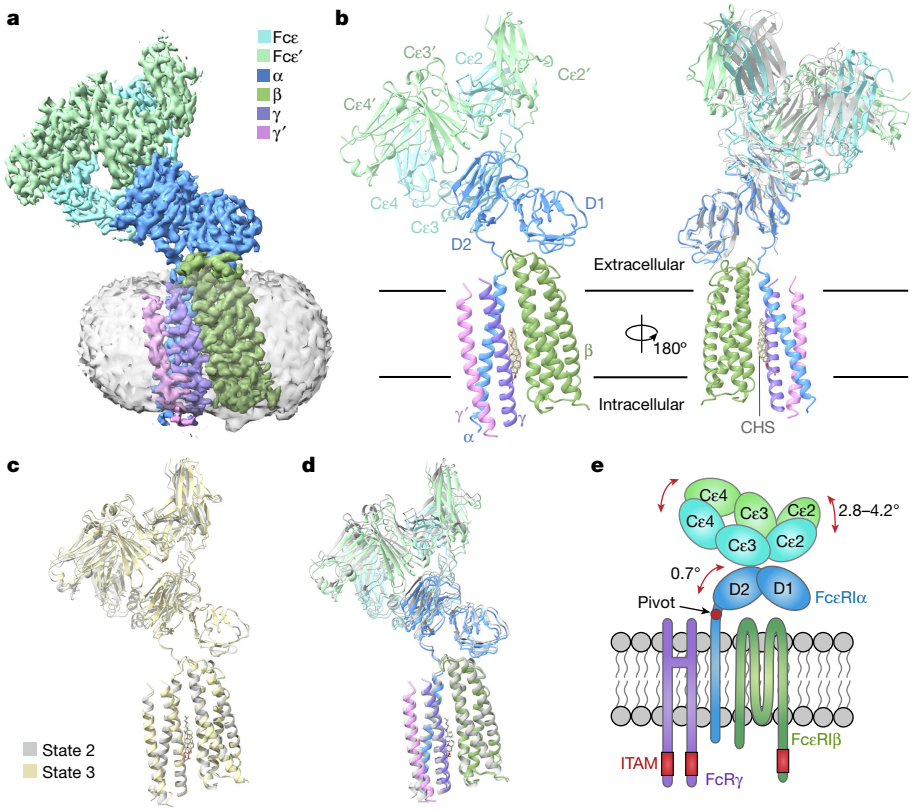

Fig. 1 | Overall structure of the rat Fcε–FcεRI complex. a, Cryo-EM reconstruction of the rat Fcε–FcεRI complex (state 1). The two chains of Fcε, FcεRIα, FcεRIβ and the two chains of FcRγ are shown in cyan, light green, blue, green, purple and magenta, respectively. The detergent micelle is depicted in transparent grey. **b**, Two views of a ribbon rendering of the rat Fcε–FcεRI structure. The structural model of CHS and the corresponding EM density are shown as sticks and meshes, respectively. In the right panel, the human Fcε–sFcεRIα crystal structure (Protein Data Bank (PDB) ID: 2Y7Q), shown in light grey, is superimposed onto the rat Fcε–FcεRI structure for comparison. **c**, State 2 and state 3 of the rat Fcε–FcεRI structures determined using the endogenous FcεRI complex from RBL-2H3 cells. **d**, Structural comparison of state 1 and state 2 Fcε–FcεRI complexes. State 1 is shown in the same colours as in **b**, whereas state 2 is shown in grey. **e**, A schematic representation of the Fcε–FcεRI complex structure, illustrating that slight rigid-body movements can occur in the Cε2 and Cε4 domains of Fcε, as well as in the extracellular region of FcεRI.

Cryo-EM structure of the Fcε–FcεRI complex

To decipher the molecular underpinnings of the FcεRI complex, we first produced recombinant human FcεRI in HEK293F cells through the co-expression of FcεRIα, FcεRIβ and FcRγ. The FcεRI complex was solubilized and purified using a combination of lauryl maltose neopentyl glycol and cholesterol hemisuccinate (CHS), and was then used to reconstitute a complex with human Fcε (Extended Data Fig. 1a,b). The cryogenic electron microscopy (cryo-EM) structure of this Fcε–FcεRI assembly was subsequently determined to a resolution of 3.6 Å (Extended Data Fig. 2 and Extended Data Table 1). The 1:1 Fcε/FcεRIα interaction is consistent with previous crystallographic data[19,20]. The Cε3–Cε4 segment of Fcε, along with sFcεRIα and the corresponding Fcε–sFcεRIα interface, closely resembles the crystal structure of the Fcε–sFcεRIα complex (Extended Data Fig. 2i). The Cε2 domains, which are not directly involved in interacting with FcεRIα, exhibit rotations of 2.5° and 6.8°, reminiscent of the flexibility of Cε2 relative to Cε3–Cε4 as observed previously[21]. Nonetheless, the TM region of FcεRIα, as well as those of the FcεRIβ and FcRγ subunits, was unresolved in the cryo-EM density map, probably owing to the flexibility of the extracellular region in relation to the TM segments.

The three subunits of FcεRI are evolutionarily conserved in mammals, especially in the TM regions (Extended Data Fig. 3). Murine FcεRI exists exclusively as an αβγ2 tetramer, with the FcεRIβ subunit being critical for the cell surface expression of FcεRIα (ref. 22). This observation led us to reason that murine FcεRIβ may establish a more robust interaction with FcεRIα, thus facilitating structural characterization. Consequently, we reconstituted rat and mouse FcεRI complexes. Rat FcεRI showed a higher expression level and less aggregation during purification when compared to the mouse counterpart. The rat Fcε–FcεRI complex was subsequently prepared (Extended Data Fig. 1c,d) and used for further cryo-EM analysis, and a final reconstruction at an average resolution of 2.9 Å was achieved (Extended Data Fig. 4 and Extended Data Table 1). To further improve the density quality of the TM region, a mask-based local refinement was implemented, allowing for accurate model building and the assignment of side chains (Extended Data Fig. 5). The final structural model includes the Fcε, the ectodomain and TM helix of FcεRIα, and the TM regions of FcεRIβ and FcRγ. Portions of the cytosolic regions of FcεRIα, FcεRIβ and FcRγ were also observed extending from the TM regions; nevertheless, the ITAM regions in FcεRIβ and FcRγ were not visualized in the density map.

The rat Fcε–FcεRI complex adopts a tree-like structure (Fig. 1a), with Fcε binding asymmetrically to the arch formed by the extracellular domain of FcεRIα, similar to the human Fcε–sFcεRIα crystal structure (Fig. 1b). FcεRIα, FcεRIβ and FcRγ are organized in a 1:1:2 stoichiometry to form a heterotetramer, with FcεRIα positioned at the centre of the assembly. The extracellular region of FcεRIα inclines towards the membrane side and juxtaposes FcεRIβ. Within the TM region, the single TM helix of FcεRIα coalesces with the FcRγ dimer (the two FcRγ subunits are designated as FcRγ and FcRγ′, respectively) to form a three-helix bundle, which further engages with FcεRIβ through extensive interactions. In addition, strong density was observed between FcεRIα,

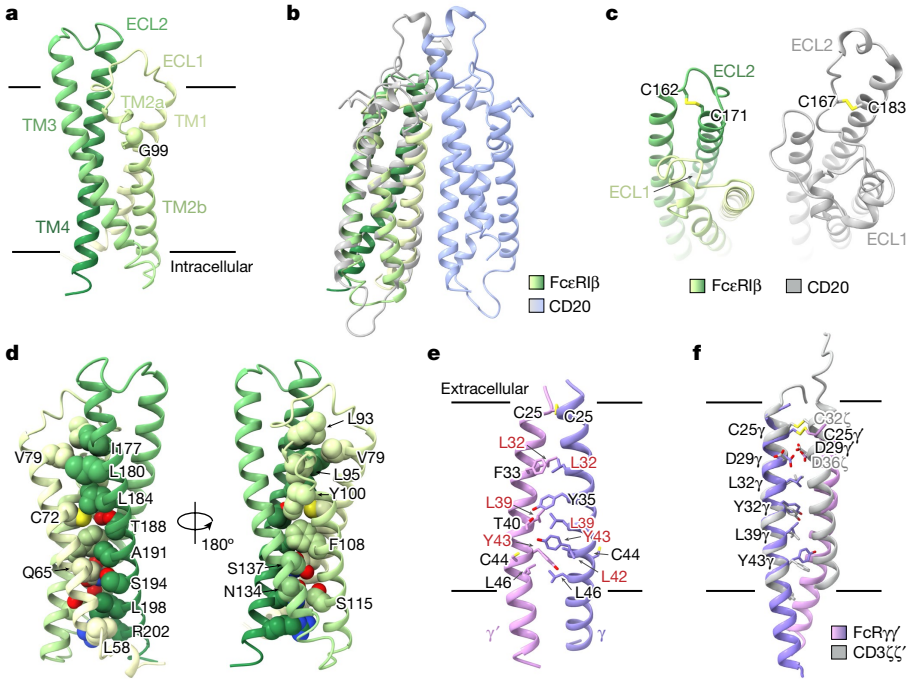

Fig. 2 | Structures of FcεRIβ and FcRγ. a, Ribbon diagram of the FcεRIβ structure. **b**, Structural overlay of FcεRIβ on one subunit (grey) in the CD20 homodimer (PDB ID: 6VJA). The other CD20 molecule is shown in blue. **c**, Structural comparison of the extracellular regions of FcεRIβ and CD20. **d**, The TM helices of FcεRIβ form a tightly packed bundle. The side chains of residues packing along the central axis of TM bundle are shown in space-filling representations. **e**, Structure of the FcRγ dimer. Residues that are mutated in this study are highlighted in red. **f**, Structural comparison between the FcRγ homodimer and CD3ζ homodimer (PDB ID: 7FJD), with the CD3ζ dimer shown in grey. In the FcRγ and CD3ζ molecules shown on the right, only Cys25 and Asp29 in the FcRγ molecule, as well as Cys32 and Asp36 in the CD3ζ molecule are shown with side chains.

FcεRIβ and FcRγ in the intracellular half of the TM region (Fig. 1b and Extended Data Fig. 5b). This density closely resembled that of a cholesterol molecule and was designated as CHS, given its presence in the buffer. The presence of this cholesterol-like moiety further enhances the interaction between FcεRIβ and FcεRIα–FcRγ.

To further corroborate the structure of the rat Fcε–FcεRI complex, we isolated endogenous FcεRI from RBL-2H3 rat basophilic leukaemia cells, which express a high level of FcεRI (ref. 23), and then examined the resulting Fcε–FcεRI complex using cryo-EM (Extended Data Fig. 6 and Extended Data Table 1). Two slightly different structures, referred to as state 2 and state 3, were reconstructed, both achieving a global resolution of approximately 3.0 Å. These structures exhibit striking similarity, with the entire FcεRI tetramer from one structure aligning closely with the other, showing a root-mean-square deviation of 1.0 Å (Fig. 1c). Notably, the Fcε–FcεRI interfaces remain unchanged. The most notable variance between the two structures is observed in the non-contacting Cε2 and Cε4 domains of Fcε, which pivot around the Cε3 pair that engage FcεRI by 2.8–4.2°. Moreover, both structures closely resemble the structure determined using recombinant FcεRI described above (state 1; Fig. 1d), particularly in the TM region, and can be overlapped with the TM of the state 1 structure with a root-mean-square deviation of 0.7–0.8 Å. Densities corresponding to the cholesterol moiety are also evident in both state 2 and state 3 structures, positioned similarly between FcεRIβ and FcεRIα–FcRγ as in state 1 (Fig. 1c). Compared to state 2 and state 3, state 1 exhibits a 0.7° tilt of the extracellular region of FcεRI relative to the TM segments, which propagates to Fcε and leads to a rigid-body movement of the Fcε–sFcεRIα en bloc (Fig. 1e). This conformational change does not affect the Fcε–FcεRI interface or the interface between the extracellular regions of FcεRIα and FcεRIβ. Collectively, these cryo-EM structures offer a detailed view of the Fcε–FcεRI architecture. Given the high quality of the state 1 structure, our subsequent structural analysis will focus on this structure.

Structures of FcεRIβ and FcRγ

FcεRIβ (also known as MS4A2) is a member of the membrane-spanning 4A (MS4A) protein family, characterized by a quartet of TM helices[24]. The prototypical member of this family is the B cell antigen CD20 (also known as MS4A1). The core structure of FcεRIβ has a comparable architecture to that of CD20, with four TM helices (TM1–TM4) arranged in a clockwise manner when viewed from the extracellular side, and both the amino and carboxy termini situated on the intracellular side (Fig. 2a,b). A notable kink in TM2, attributed to Gly99, bifurcates it into TM2a and TM2b. The MS4A proteins contain two extracellular loops (ECL1 and ECL2). Despite highly variable ECL sequences among MS4A proteins, a conserved disulfide bond links Cys162 in ECL2 to Cys171 at the onset of TM4 in FcεRIβ, analogous to the Cys167–Cys183 bond in CD20 (Fig. 2c). A critical distinction between CD20 and FcεRIβ is the oligomeric state. CD20 forms a homodimer[25,26], whereas FcεRIβ is monomeric within the FcεRI complex (Fig. 2b). In CD20, TM1 and TM4 contribute to dimerization, whereas in FcεRIβ, these helices interface with FcεRIα and FcRγ. As in CD20, the TM helices of FcεRIβ are densely packed, featuring central-axis interactions involving specific residues such as Leu58, Gln65, Cys72, Val79 (TM1); Leu93, Leu95 (TM2a); Tyr100, Phe108, Ser115 (TM2b); Asn134, Ser137 (TM3); Ile177, Leu180, Leu184, Thr188, Ala191, Ser194, Leu198 and Arg202 (TM4; Fig. 2d).

The FcRγ molecule was initially identified as the third component of the FcεRI complex and was subsequently recognized for its key signalling role within a variety of other immune receptor complexes. The two chains of the FcRγ dimer, namely FcRγ and FcRγ′, form a disulfide-linked dimer through Cys25 (Fig. 2e). By contrast, the Cys44 residues on both FcRγ chains are oriented away from the dimer interface, and are not participating in disulfide bond formation. Besides Cys25, several other residues in FcRγ contribute to the dimer formation, including Leu32γ,

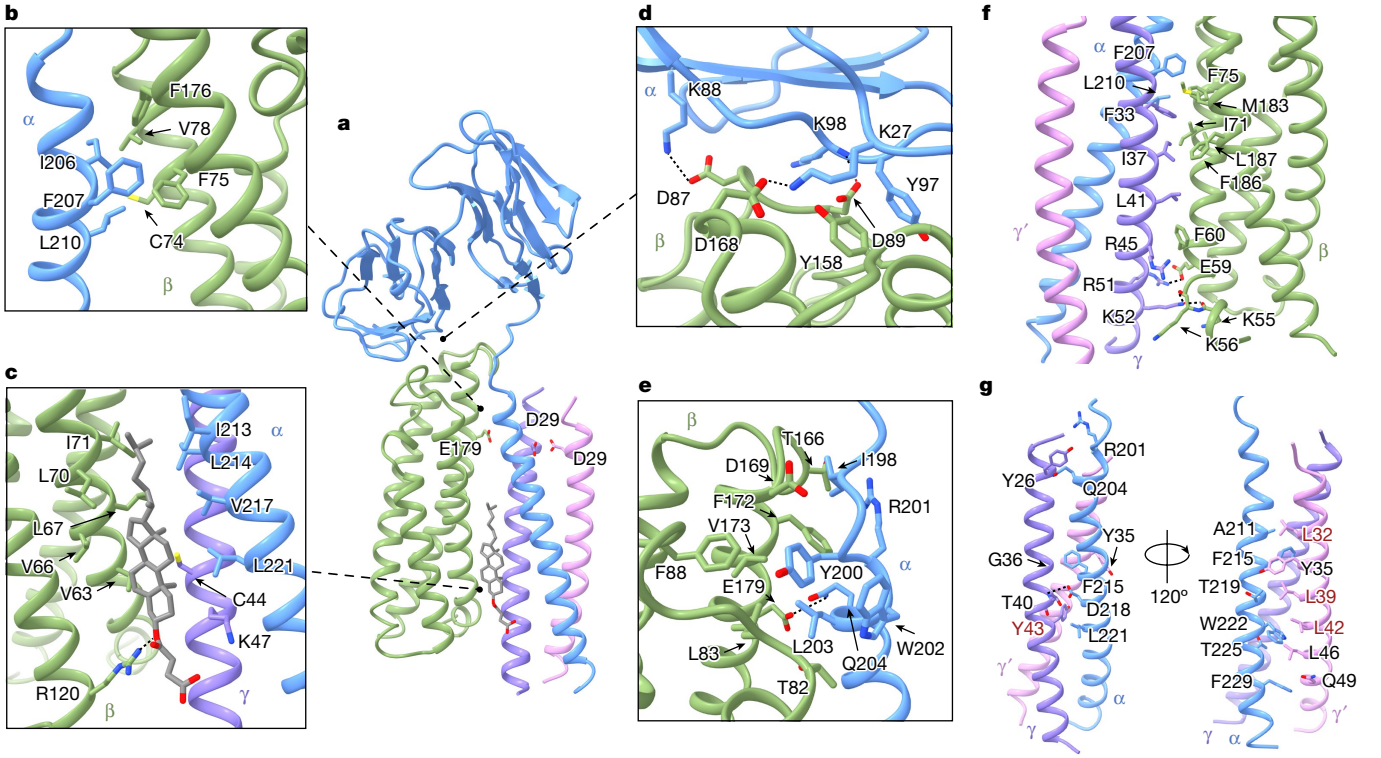

Fig. 3 | Molecular assembly of the rat FcεRI complex. a, Ribbon diagram of the FcεRI complex. Asp29γ, Asp29γ′ and Glu179β are shown with their side chains. **b**, Interactions between FcεRIα and FcεRIβ in the TM region. **c**, The cholesterol moiety interacting with FcεRIα, FcεRIβ and FcRγ to reinforce the FcεRI assembly. **d**, Interaction between the extracellular region of FcεRIα and FcεRIβ. Polar interactions are indicated with dashed lines. **e**, Interaction between the juxtamembrane region of FcεRIα and FcεRIβ. **f**, Interaction between the FcRγ chain and the TM regions of FcεRIα and FcεRIβ. **g**, Interaction between the FcRγ dimer and the TM of FcεRIα.

Leu32γ′, Phe33γ′, Tyr35γ, Leu39γ, Leu39γ′, Thr40γ′, Leu42γ, Tyr43γ, Tyr43γ′, Leu46γ and Leu46γ′. It is noteworthy that the FcRγ dimer is asymmetric, as the two subunits contribute non-identical sets of residues to the interface. This asymmetry stems from the interaction between the FcRγ dimer and the FcεRIα TM, leading to the formation of a three-stranded coiled-coil structure. The TM region of FcRγ is highly homologous to that of CD3ζ (ref. 18). A structural comparison revealed that the TM regions of FcRγ and CD3ζ indeed exhibit remarkable similarities, albeit with some differences in their respective dimer arrangements (Fig. 2f). The positioning of the Cys25–Cys25 disulfide bond in FcRγ is analogous to that of the Cys32–Cys32 disulfide bond in CD3ζ. Additionally, Asp29 in FcRγ corresponds well with Asp36 in CD3ζ, which is a crucial residue for interaction with TCRα Arg253 within the TCR–CD3 complex.

Molecular mechanism of FcεRI assembly

The high-resolution cryo-EM structure elucidates the assembly mechanism of FcεRI (Fig. 3a). FcεRIα is pivotal in orchestrating the assembly, establishing interactions with FcεRIβ and the two FcRγ chains. The N-terminal portion of the FcεRIα TM helix packs with TM1 and TM4 of FcεRIβ (Fig. 3b). Residues such as Ile206α, Phe207α and Leu210α from FcεRIα engage in hydrophobic and van der Waals interactions with Cys74β, Phe75β and Val78β from FcεRIβ-TM1, as well as Phe176β from FcεRIβ-TM4. The critical role of FcεRIβ-TM1 in interacting with FcεRIα has been demonstrated by truncation studies[27]. The TM domain of FcεRIα is angled in relation to that of FcεRIβ, resulting in the formation of a tunnel near the cytoplasmic side. The cholesterol moiety of CHS wedges into this tunnel and interacts with FcεRIα, FcεRIβ and the FcRγ chain to strengthen the structural integrity of the FcεRI complex (Fig. 3c). The cholesterol group's hydrocarbon tail is surrounded by Ile213α and Leu214α from FcεRIα, and Leu70β and Ile71β from FcεRIβ. The tetracyclic ring nestles within a pocket formed by Val217α and Leu221α from FcεRIα, Val63β, Val66β and Leu67β from FcεRIβ, and Cys44γ and Lys47γ from FcRγ. Furthermore, the monoester oxygen of CHS, which corresponds to the hydroxyl group oxygen of cholesterol, is coordinated by Arg120β.

The extracellular region of FcεRIα also engages in contacts with FcεRIβ (Fig. 3d). The D1 domain of FcεRIα folds over and makes extensive contacts with the two ECLs of FcεRIβ. For example, Lys27α interacts with Tyr158β and Asp168β in ECL2. Lys88α interacts with Asp87β in ECL1. Tyr97α packs against Tyr158β, and along with Lys98α, accommodates Asp89β. Additional interactions occur at the juxtamembrane region (Fig. 3e): Ile198α is surrounded by van der Waals interactions from Thr166β–Asp169β, and together with Arg201α, they enclose Phe172β. Tyr200α packs against Phe88β and Val173β. Trp202α and Leu203α interact with Thr82β and Leu83β, respectively. Moreover, Gln204α forms a hydrogen bond with Glu179β. It should be noted that unlike residues in the TM regions, these FcεRIα and FcεRIβ residues are only partially conserved between human and rat sequences (Extended Data Fig. 3). This partial conservation suggests that the interaction between the extracellular regions of human FcεRIα and FcεRIβ may not be as rigid, offering a possible explanation for the flexibility of the extracellular region in relation to the TM region observed in the human FcεRI sample.

The two chains of FcRγ assume asymmetrical roles within the FcεRI complex, interacting distinctly with FcεRIα and FcεRIβ, which is reminiscent of how the two CD3ζ molecules are arranged in the TCR complex. The FcRγ chain plays a more dominant role, forms extensive interfaces with both FcεRIα and FcεRIβ (Fig. 3f), and shields approximately 800 and 740 Å^2 of surface area on each molecule. Phe33γ is surrounded by a cluster of hydrophobic residues including Phe207α, Leu210α, Phe75β

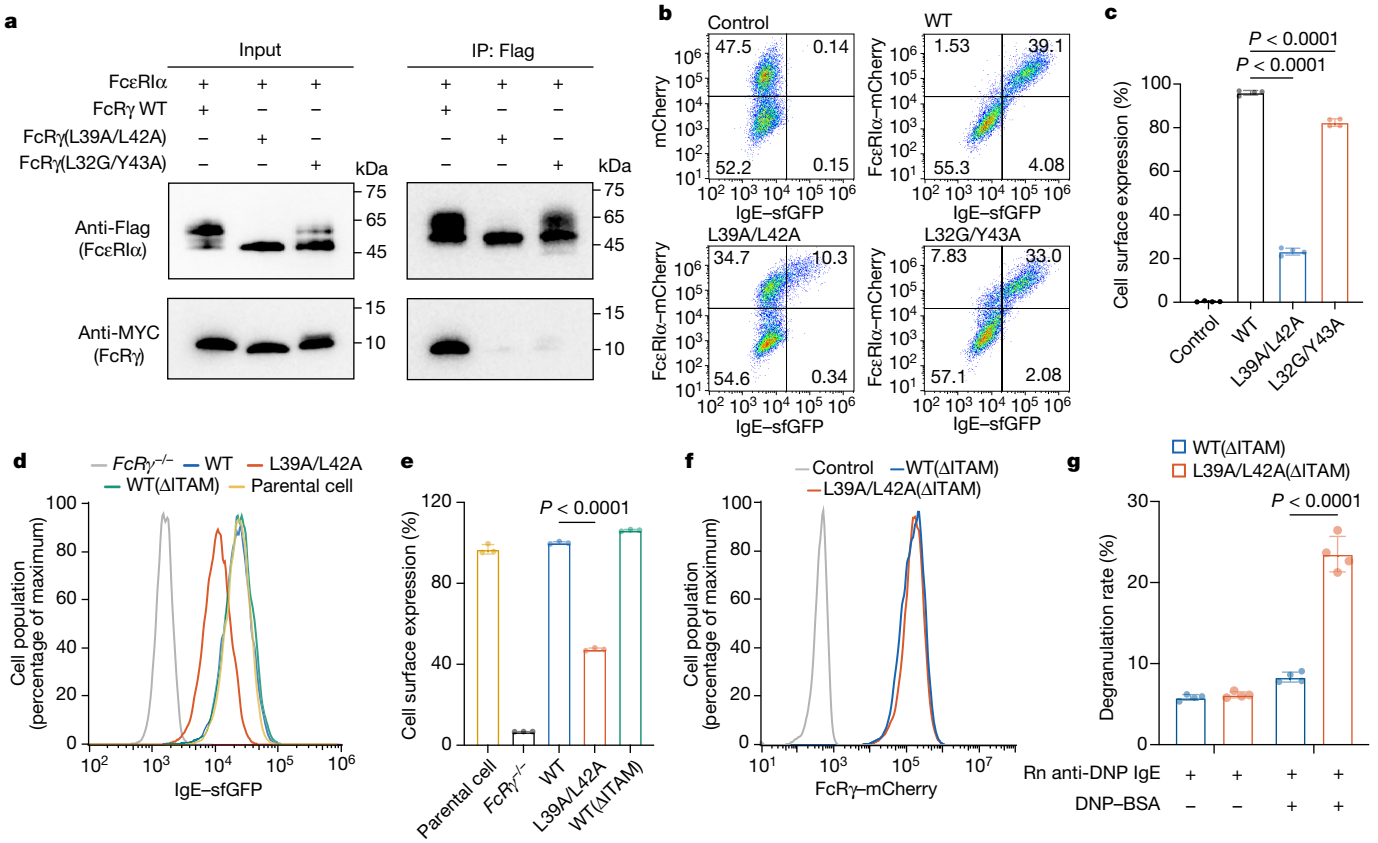

Fig. 4 | FcRγ mutants abolish the function of FcεRI. a, The human FcRγ mutants were defective in binding to FcεRIα. The immunoprecipitation (IP) experiments were repeated at least two times with similar results. For gel source data in this paper, see Supplementary Fig. 1. **b**, Flow cytometry analyses suggested that the human FcRγ mutants caused decreases of FcεRIα cell surface expression. Representative flow cytometry plots are shown. The cells were sorted based on the expression levels and cell surface levels of FcεRIα, and the numbers in the flow cytometry plots indicate the percentages of cells in different groups. sfGFP, superfolder GFP. **c**, Quantification analyses of the flow cytometry experiments in **b**. The dots indicate individual data points for $n = 4$ biologically independent replicates. **d**, WT FcRγ or the WT(ΔITAM) variant effectively restored the cell surface presentation of endogenous FcεRIα in *FcRγ*$^{-/-}$ RBL-2H3 cells, whereas the L39A/L42A mutant only partially restored FcεRIα levels. **e**, Quantification analyses of the flow cytometry experiments in **d**. The dots indicate individual data points for $n = 3$ biologically independent replicates. **f**, Flow cytometry analyses demonstrated that WT(ΔITAM) and L39A/L42A/ΔITAM FcRγ exhibited similar expression levels in RBL-2H3 cells. **g**, WT(ΔITAM), but not L39A/L42A/ΔITAM, suppressed RBL-2H3 cell degranulation. The dots indicate individual data points for $n = 4$ biologically independent replicates. Rn, *Rattus norvegicus*. BSA, bovine serum albumin. Data in **c**,**e**,**g** are presented as mean ± s.d. *P* values in **c**,**e**,**g** were calculated using one-way analysis of variance followed by Dunnett's multiple-comparison test using GraphPad Prism 9.

and Met183β, whereas Ile37γ is surrounded by Ile71β, Phe186β and Leu187β. Leu41γ and Arg45γ clamp onto Phe60β. Arg51γ and Lys52γ also engage with the N-terminal intracellular region of FcεRIβ, forming hydrophilic interactions with Glu59β and the peptide backbone of Lys55β–Lys56β. Furthermore, Tyr26γ forms interactions with Arg201α and Gln204α in FcεRIα (Fig. 3g). Gly36γ and Tyr35γ′ together anchor Phe215α. Thr40γ helps neutralize the negative charge of Asp218α through its main chain amino group, thereby enhancing the stability of the complex. Indeed, previous modelling analyses have suggested close spatial proximity of Thr40γ and Asp218α (ref. 28). FcRγ′ is positioned at the periphery and exclusively interacts with FcεRIα (Fig. 3g), concealing 470 Å^2 of the surface of FcεRIα. Tyr35γ′, Leu39γ′, Leu42γ′, Leu46γ′ and Gln49γ′ pack against Tyr215α, Thr219α, Trp222α, Thr225α and Phe229α, reinforcing the FcRγ dimer's association with FcεRIα. The conserved F-x-x-(D or N)-T motif in FcγRIIIA and FcεRI is integral to their binding to FcRγ (ref. 29). Indeed, Phe215, Asp218 and Thr219 in rat FcεRIα are all critically involved in interacting with the two FcRγ subunits.

The FcεRI structure lacks a positively charged residue to coordinate with Asp29γ and Asp29γ′. These aspartate residues are situated at a comparable level to Glu179β, creating an acidic layer within the TM region (Fig. 3a). As these negatively charged residues lie proximal to the plasma membrane's outer surface, Asp29γ and Asp29γ′ may directly interact with solvent molecules.

FcRγ mutants abolish the function of FcεRI

To ascertain the importance of the interactions identified in the cryo-EM structure for the functionality of the FcεRI complex, we first engineered substitutions into human FcRγ and evaluated their impact on the association of FcRγ with human FcεRIα. The mutants L39A/L42A and L32G/Y43A both exhibited diminished binding to FcεRIα in co-immunoprecipitation assays (Fig. 4a), underscoring the pivotal roles of these amino acids in FcRγ dimerization and its interaction with FcεRIα (Figs. 2e and 3g). Additionally, co-expression of FcεRIα with these mutants led to a remarkable reduction in FcεRIα glycosylation, as indicated by altered electrophoretic migration patterns (Fig. 4a). This suggests that the mutants impair the proper processing of FcεRIα within the secretory pathway.

The cell surface expression of human FcεRIα relies on the presence of FcRγ (ref. 30). It has also been shown that FcRγ Leu39 (Leu21 in the mature protein) is critical for the surface presentation of the FcεRI αγ2 complex[31]. In line with these findings, analysis of the binding of

a green fluorescent protein (GFP)-tagged human IgE through flow cytometry showed that FcεRIα was detected on the surface of HEK293T cells only when it was co-expressed with wild-type (WT) FcRγ (Fig. 4b,c and Extended Data Fig. 7). Conversely, co-expression of the L39A/L42A mutant resulted in a substantial reduction in the cell surface level of FcεRIα. Co-expression with the L32G/Y43A mutant also led to a modest decrease in the cell surface level of FcεRIα.

To further investigate the impact of these FcRγ mutants within a context more relevant to IgE biology, we generated *FcRγ*-knockout (*FcRγ*$^{-/-}$) RBL-2H3 cells using the CRISPR–Cas9 technique following an established protocol[32]. We then generated *FcRγ*$^{-/-}$ cells stably expressing WT or mutant FcRγ. Consistent with the results observed in HEK293T cells, our data show that the expression of WT FcRγ or the WT(ΔITAM) variant, which contains an intact TM region but lacks the cytoplasmic ITAM motif, effectively restored the cell surface presentation of endogenous FcεRIα in RBL-2H3 cells, as indicated by the binding of a GFP-tagged rat IgE (Fig. 4d,e). By contrast, the L39A/L42A mutant only partially restored FcεRIα levels and IgE binding. The L32G/Y43A mutant exhibited markedly lower expression levels in RBL-2H3 cells (Extended Data Fig. 7e), precluding an assessment of its effect on FcεRIα levels in these cells.

The engagement of the IgE–antigen complex with FcεRI triggers the degranulation of mast cells and basophils, resulting in the release of pro-inflammatory agents that are central to allergic reactions. To investigate the impact of specific FcRγ alterations on IgE-mediated degranulation, we engineered RBL-2H3 cells stably expressing the WT(ΔITAM) or L39A/L42A/ΔITAM mutant of FcRγ. Our hypothesis was that the WT(ΔITAM) FcRγ variant would compete with the endogenous FcRγ for FcεRIα binding, yet the absence of the ITAM would render the FcεRI complex inactive, consequently inhibiting FcεRI signalling. To assess degranulation, we produced an anti-dinitrophenyl (DNP) IgE by substituting the Fcε region of mouse SPE-7 IgE (ref. 33) with rat Fcε. Degranulation was quantified by measuring β-hexosaminidase release. Expression levels of WT(ΔITAM) and L39A/L42A/ΔITAM were comparable (Fig. 4f). However, after sensitization with anti-DNP IgE and stimulation with DNP-conjugated bovine serum albumin, WT(ΔITAM) cells exhibited a marked reduction in β-hexosaminidase release (Fig. 4g). By contrast, cells expressing L39A/L42A/ΔITAM showed no significant impact on degranulation. Together, these findings corroborate our structural analyses and underscore the indispensable role of FcRγ in the functional integrity of the FcεRI complex.

Interaction between FcRγ and other FcRs

Besides FcεRI, other activating Fc receptors including FcγRI, FcγRIIIA and FcαRI also rely on FcRγ to initiate antibody effector functions (Fig. 5a). The TM regions of FcεRIα, FcγRI and FcγRIIIA share a high degree of similarity with each other (Fig. 5b). They all lack a positively charged residue in their TM regions, and the conserved F-x-x-(D or N)-T sequences in FcγRIIIA and FcεRI are crucial for their interaction with FcRγ (ref. 29). The two FcRγ mutants, L39A/L42A and L32G/Y43A, were both impaired in their ability to bind human FcγRIIIA (Fig. 5c), similar to their inabilities to associate with FcεRIα. Furthermore, when co-expressed with these mutants, FcγRIIIA was not efficiently transported to the cell surface (Fig. 5d,g), as FcRγ is also essential for the surface expression of FcγRIIIA, as it is for FcεRIα (refs. 34,35). It is worth noting that the L39A/L42A alteration led to a more pronounced decrease in the cell surface expression of FcεRIα compared to L32G/Y43A (Fig. 4c), whereas its impact on the surface expression of FcγRIIIA was more moderate and similar to that of L32G/Y43A (Fig. 5g). These distinct effects of the L39A/L42A mutant on the cell surface expression of FcεRIα and FcγRIIIA indicate that subtle differences still exist in the interaction modes of FcεRIα–FcRγ and FcγRIIIA–FcRγ.

By contrast, the FcαRI–FcRγ interaction exhibits more divergent features[31,36]. The TM of FcαRI does not show substantial homology to the TM regions of FcεRIα, FcγRI and FcγRIIIA, and contains an arginine residue that is characteristically present in several other activating LRC receptors that engage with FcRγ (Fig. 5b). Additionally, FcαRI does not require FcRγ for cell surface expression[37,38]. Indeed, even when co-expressed with the two FcRγ mutants, FcαRI is efficiently delivered to the cell surface (Fig. 5f,h). Examination of the interactions between FcαRI and the FcRγ mutants showed that L39A/L42A still seemed to retain interaction with FcαRI, whereas L32G/Y43A was completely unable to bind FcαRI (Fig. 5e). These results suggest that the FcαRI–FcRγ interaction mode is probably fundamentally different when compared to the interactions between FcRγ and FcεRIα or FcγRIIIA.

Discussion

In this study, we unveil the cryo-EM structure of the FcεRI signalling complex, shedding light on the molecular intricacies of its assembly. Our findings corroborate previous research[10,11], demonstrating that the FcεRI complex is organized in a 1:1:2 stoichiometry with FcεRIα at the core. Notably, we show that FcεRIβ adopts a compact four-helix bundle structure, with the close packing of its four TMs suggesting that FcεRIβ, akin to CD20 (ref. 25), may not function as a calcium channel, contradicting certain speculations[24] but aligning with previous analyses[39,40].

We further show that a cholesterol-like molecule, located at a position corresponding to the inner leaflet of the membrane, facilitates the interaction between FcεRIβ and FcεRIα–FcRγ. Recent advancements have led to the determination of the structures of several αβ and γδ TCR–CD3 complexes[41–45]. Cholesterol molecules were observed in both the outer and inner leaflets of the membrane in the αβ TCR–CD3 (Extended Data Fig. 8a; ref. 42). The outer-leaflet cholesterol seems to be consistently present and probably fulfils a structural role[43,44], whereas the inner-leaflet cholesterol seems to exert a regulatory effect by inhibiting TCR signalling[42]. In the γδ TCR–CD3 structures, the inner-leaflet cholesterol densities are more prominent (Extended Data Fig. 8b), and mutational analyses suggest a similar inhibitory role for this cholesterol[45]. Whereas the TM helices of both αβ and γδ TCR–CD3 complexes are oriented nearly perpendicular to the membrane, the TM of FcεRIα is oriented differently relative to FcRγ, obstructing the binding of outer-leaflet cholesterol (Extended Data Fig. 8a,b). Previous research has indicated that FcεRI signalling is disrupted following pharmacological removal of cholesterol[46], consistent with a stabilizing role for the cholesterol in our current structure. The potential regulatory impact of this inner-leaflet cholesterol on FcεRI function warrants further investigation.

FcRγ can substitute CD3ζ to form a unconventional TCR complex[47–49]. Similarly, both the homodimer of CD3ζ and the CD3ζ–FcRγ heterodimer are capable of binding to FcγRIIIA on natural killer cells[6,50]. Apart from their highly homologous TM regions, CD3ζ and FcRγ possess distinct features. In the αβ TCR–CD3 structure, the extracellular region of one CD3ζ interacts closely with the membrane-proximal connecting peptides of TCRα and CD3δ (Extended Data Fig. 8a; ref. 41). In the Vγ9Vδ2 γδ TCR–CD3 structure, a similar albeit less extensive interaction is observed with the connecting peptides of TCRδ2 and CD3δ (Extended Data Fig. 8b; ref. 45). In comparison to that of CD3ζ, the N-terminal extracellular region of FcRγ is shorter (Extended Data Fig. 8c), and was not observed in the FcεRI structure. These distinctions could potentially affect the functionality of FcRγ and CD3ζ.

Through functional mutagenesis analysis, we further establish that the interaction of FcRγ with FcεRIα probably parallels its interaction with FcγRIIIA, but diverges from its interaction with FcαRI. TCRα has an arginine residue (Arg253) in the TM region, which engages in interaction with Asp36 of CD3ζ in the TCR–CD3 complex (Fig. 5i). Given the correspondence between Asp29 in FcRγ and Asp36 in CD3ζ (Fig. 2f), it is plausible that FcRγ could interact with TCRα in a manner reminiscent of the TCRα–CD3ζ interaction in the unconventional TCR complexes involving FcRγ. Furthermore, considering that FcαRI also features a

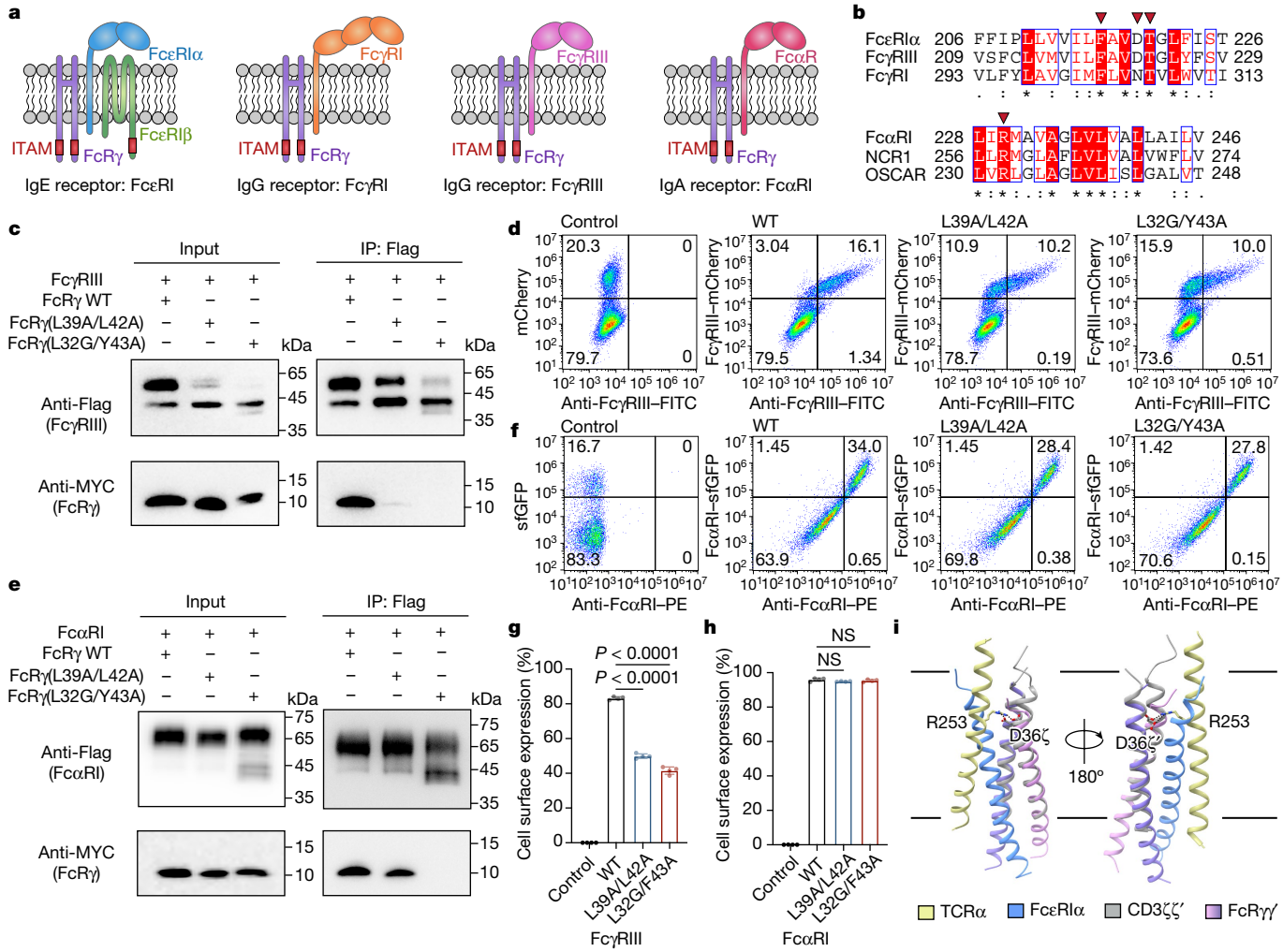

Fig. 5 | Interaction between FcRγ and other Fc receptors. a, A schematic representation of FcRγ interacting with other FcRs. **b**, Sequence alignment of the TM regions of FcεRIα, FcγRI and FcγRIIIA, as well as sequence alignment of the TM regions of FcαRI, NCR1 and OSCAR. The asterisks, double dots and single dots indicate fully conserved, strongly conserved and weakly conserved residues, respectively. **c**, The human FcRγ(L39A/L42A) and FcRγ(L32G/Y43A) mutants were defective in binding to FcγRIIIA. **d**, Representative flow cytometry plots for the analysis of FcγRIIIA cell surface expression. FITC, fluorescein isothiocyanate; PE, phycoerythrin. **e**, The L39A/L42A mutant exhibited a modest defect in interacting with FcαRI, whereas the L32G/Y43A mutant is completely defective. The immunoprecipitation experiments in **c**,**e** were repeated at least two times with similar results. **f**, Representative flow cytometry plots for the analysis of FcαRI cell surface expression. **g**, Statistical analyses of FcγRIIIA cell surface expression. Dots indicate individual data points for $n = 4$ biologically independent replicates. **h**, Statistical analyses of FcαRI cell surface expression. Dots indicate individual data points for $n = 4$ biologically independent replicates. NS, not significant. Data in **g**,**h** are presented as mean ± s.d. *P* values in **g**,**h** were calculated using one-way analysis of variance followed by Dunnett's multiple-comparison test using GraphPad Prism 9. **i**, Structural comparison between FcεRIα–FcRγγ′ and TCRα–CD3ζζ′ (PDB ID: 7FJD). The two structures are superimposed by aligning the FcRγγ′ and CD3ζζ′ dimers. Arg253 from TCRα and Asp36 from the two CD3ζ chains are highlighted with their side chains shown.

characteristic arginine residue within its TM (Fig. 5b), it is tempting to speculate that FcRγ might engage with FcαRI in a similar fashion, involving the TM arginine residue of FcαRI and Asp29 in FcRγ, which does not participate in the interaction with FcεRIα.

The interaction between antigens and IgE triggers the activation of FcεRI, leading to allergic responses. However, the molecular mechanism by which antigen binding induces structural changes in the subunits of FcεRI remains elusive. A comparison of the architecture of rat and human FcεRI suggests variations in rigidity, with human FcεRI exhibiting more flexibility in the relative arrangements between its extracellular and TM regions. The implications of these structural differences on antigen sensitivity and signalling strength also remain unclear. Nevertheless, the rat FcεRI structure provides a foundation for future research aimed at deciphering the signalling mechanism of FcεRI. Additionally, our findings shed light on the functioning of other immune receptors dependent on FcRγ.

Online content

Any methods, additional references, Nature Portfolio reporting summaries, source data, extended data, supplementary information, acknowledgements, peer review information; details of author contributions and competing interests; and statements of data and code availability are available at https://doi.org/10.1038/s41586-024-07864-5.

1. Galli, S. J. & Tsai, M. IgE and mast cells in allergic disease. *Nat. Med.* **18**, 693–704 (2012).
2. McDonnell, J. M., Dhaliwal, B., Sutton, B. J. & Gould, H. J. IgE, IgE receptors and anti-IgE biologics: protein structures and mechanisms of action. *Annu. Rev. Immunol.* **41**, 255–275 (2023).
3. Kinet, J. P. The high-affinity IgE receptor (Fc epsilon RI): from physiology to pathology. *Annu. Rev. Immunol.* **17**, 931–972 (1999).
4. Martin, A. M., Kulski, J. K., Witt, C., Pontarotti, P. & Christiansen, F. T. Leukocyte Ig-like receptor complex (LRC) in mice and men. *Trends Immunol.* **23**, 81–88 (2002).
5. Humphrey, M. B., Lanier, L. L. & Nakamura, M. C. Role of ITAM-containing adapter proteins and their receptors in the immune system and bone. *Immunol. Rev.* **208**, 50–65 (2005).

6. Nimmerjahn, F. & Ravetch, J. V. Fcgamma receptors as regulators of immune responses. *Nat. Rev. Immunol.* **8**, 34–47 (2008).
7. Hogarth, P. M. & Pietersz, G. A. Fc receptor-targeted therapies for the treatment of inflammation, cancer and beyond. *Nat. Rev. Drug Discov.* **11**, 311–331 (2012).
8. Brandsma, A. M., Hogarth, P. M., Nimmerjahn, F. & Leusen, J. H. Clarifying the confusion between cytokine and Fc receptor "common gamma chain". *Immunity* **45**, 225–226 (2016).
9. Bruhns, P. & Jonsson, F. Mouse and human FcR effector functions. *Immunol. Rev.* **268**, 25–51 (2015).
10. Blank, U. et al. Complete structure and expression in transfected cells of high affinity IgE receptor. *Nature* **337**, 187–189 (1989).
11. Miller, L., Blank, U., Metzger, H. & Kinet, J. P. Expression of high-affinity binding of human immunoglobulin E by transfected cells. *Science* **244**, 334–337 (1989).
12. Alber, G., Miller, L., Jelsema, C. L., Varin-Blank, N. & Metzger, H. Structure-function relationships in the mast cell high affinity receptor for IgE. Role of the cytoplasmic domains and of the beta subunit. *J. Biol. Chem.* **266**, 22613–22620 (1991).
13. Lin, S., Cicala, C., Scharenberg, A. M. & Kinet, J. P. The FcεRIβ subunit functions as an amplifier of FcεRIγ-mediated cell activation signals. *Cell* **85**, 985–995 (1996).
14. Turner, H. & Kinet, J. P. Signalling through the high-affinity IgE receptor FcεRI. *Nature* **402**, B24–B30 (1999).
15. Kraft, S. & Kinet, J. P. New developments in FcεRI regulation, function and inhibition. *Nat. Rev. Immunol.* **7**, 365–378 (2007).
16. Underhill, D. M. & Goodridge, H. S. The many faces of ITAMs. *Trends Immunol.* **28**, 66–73 (2007).
17. Mócsai, A., Ruland, J. & Tybulewicz, V. L. The SYK tyrosine kinase: a crucial player in diverse biological functions. *Nat. Rev. Immunol.* **10**, 387–402 (2010).
18. Orloff, D. G., Ra, C. S., Frank, S. J., Klausner, R. D. & Kinet, J. P. Family of disulphide-linked dimers containing the ζ and η chains of the T-cell receptor and the gamma chain of Fc receptors. *Nature* **347**, 189–191 (1990).
19. Garman, S. C., Wurzburg, B. A., Tarchevskaya, S. S., Kinet, J. P. & Jardetzky, T. S. Structure of the Fc fragment of human IgE bound to its high-affinity receptor FcεRIα. *Nature* **406**, 259–266 (2000).
20. Holdom, M. D. et al. Conformational changes in IgE contribute to its uniquely slow dissociation rate from receptor FcεRI. *Nat. Struct. Mol. Biol.* **18**, 571–576 (2011).
21. Drinkwater, N. et al. Human immunoglobulin E flexes between acutely bent and extended conformations. *Nat. Struct. Mol. Biol.* **21**, 397–404 (2014).
22. Blank, U., Ra, C. S. & Kinet, J. P. Characterization of truncated alpha chain products from human, rat, and mouse high affinity receptor for immunoglobulin E. *J. Biol. Chem.* **266**, 2639–2646 (1991).
23. Passante, E. & Frankish, N. The RBL-2H3 cell line: its provenance and suitability as a model for the mast cell. *Inflamm. Res.* **58**, 737–745 (2009).
24. Mattiola, I., Mantovani, A. & Locati, M. The tetraspan MS4A family in homeostasis, immunity, and disease. *Trends Immunol.* **42**, 764–781 (2021).
25. Rougé, L. et al. Structure of CD20 in complex with the therapeutic monoclonal antibody rituximab. *Science* **367**, 1224–1230 (2020).
26. Kumar, A., Planchais, C., Fronzes, R., Mouquet, H. & Reyes, N. Binding mechanisms of therapeutic antibodies to human CD20. *Science* **369**, 793–799 (2020).
27. Singleton, T. E., Platzer, B., Dehlink, E. & Fiebiger, E. The first transmembrane region of the beta-chain stabilizes the tetrameric Fc epsilon RI complex. *Mol. Immunol.* **46**, 2333–2339 (2009).
28. Rashid, A. et al. Assessing the role of Asp 194 in the transmembrane domains of the alpha-chain of the high-affinity receptor complex for immunoglobulin E in signal transduction. *Mol. Immunol.* **48**, 128–136 (2010).
29. Blazquez-Moreno, A. et al. Transmembrane features governing Fc receptor CD16A assembly with CD16A signaling adaptor molecules. *Proc. Natl Acad. Sci. USA* **114**, E5645–E5654 (2017).
30. Kuster, H., Thompson, H. & Kinet, J. P. Characterization and expression of the gene for the human Fc receptor gamma subunit. Definition of a new gene family. *J. Biol. Chem.* **265**, 6448–6452 (1990).
31. Wines, B. D., Trist, H. M., Ramsland, P. A. & Hogarth, P. M. A common site of the Fc receptor gamma subunit interacts with the unrelated immunoreceptors FcαRI and FcεRI. *J. Biol. Chem.* **281**, 17108–17113 (2006).
32. Travers, T. et al. Combinatorial diversity of Syk recruitment driven by its multivalent engagement with FcεRIγ. *Mol. Biol. Cell* **30**, 2331–2347 (2019).
33. Bax, H. J., Bowen, H., Dodev, T. S., Sutton, B. J. & Gould, H. J. Mechanism of the antigen-independent cytokinergic SPE-7 IgE activation of human mast cells in vitro. *Sci. Rep.* **5**, 9538 (2015).
34. Hibbs, M. L. et al. Mechanisms for regulating expression of membrane isoforms of Fc gamma RIII (CD16). *Science* **246**, 1608–1611 (1989).
35. Kurosaki, T., Gander, I. & Ravetch, J. V. A subunit common to an IgG Fc receptor and the T-cell receptor mediates assembly through different interactions. *Proc. Natl Acad. Sci. USA* **88**, 3837–3841 (1991).
36. Wines, B. D., Trist, H. M., Monteiro, R. C., Van Kooten, C. & Hogarth, P. M. Fc receptor γ chain residues at the interface of the cytoplasmic and transmembrane domains affect association with FcαRI, surface expression, and function. *J. Biol. Chem.* **279**, 26339–26345 (2004).
37. Pfefferkorn, L. C. & Yeaman, G. R. Association of IgA-Fc receptors (Fc alpha R) with Fc epsilon RI gamma 2 subunits in U937 cells. Aggregation induces the tyrosine phosphorylation of gamma 2. *J. Immunol.* **153**, 3228–3236 (1994).
38. Morton, H. C. et al. Functional association between the human myeloid immunoglobulin A Fc receptor (CD89) and FcR gamma chain. Molecular basis for CD89/FcR gamma chain association. *J. Biol. Chem.* **270**, 29781–29787 (1995).
39. Fewtrell, C., Mohr, F. C., Ryan, T. A. & Millard, P. J. in *Novartis Foundation Symposia Ciba Foundation Symposium 147 - IgE, Mast Cells and the Allergic Response* (eds Chadwick, D. J. et al.) 114–132 (Wiley, 1989).
40. Metzger, H. et al. The receptor with high affinity for immunoglobulin E. *Annu. Rev. Immunol.* **4**, 419–470 (1986).
41. Dong, D. et al. Structural basis of assembly of the human T cell receptor-CD3 complex. *Nature* **573**, 546–552 (2019).
42. Chen, Y. et al. Cholesterol inhibits TCR signaling by directly restricting TCR-CD3 core tunnel motility. *Mol. Cell* **82**, 1278–1287 (2022).
43. Sušac, L. et al. Structure of a fully assembled tumor-specific T cell receptor ligated by pMHC. *Cell* **185**, 3201–3213 (2022).
44. Saotome, K. et al. Structural analysis of cancer-relevant TCR-CD3 and peptide-MHC complexes by cryoEM. *Nat. Commun.* **14**, 2401 (2023).
45. Xin, W. et al. Structures of human γδ T cell receptor–CD3 complex. *Nature* https://doi.org/10.1038/s41586-024-07439-4 (2024).
46. Sheets, E. D., Holowka, D. & Baird, B. Critical role for cholesterol in Lyn-mediated tyrosine phosphorylation of FcεRI and their association with detergent-resistant membranes. *J. Cell Biol.* **145**, 877–887 (1999).
47. Curnow, S. J., Boyer, C., Buferne, M. & Schmitt-Verhulst, A. M. TCR-associated ζ-FcεRIγ heterodimers on $CD4^{-}CD8^{-}$ $NK1.1^{+}$ T cells selected by specific class I MHC antigen. *Immunity* **3**, 427–438 (1995).
48. Enyedy, E. J. et al. Fc epsilon receptor type I gamma chain replaces the deficient T cell receptor zeta chain in T cells of patients with systemic lupus erythematosus. *Arthritis Rheum.* **44**, 1114–1121 (2001).
49. Krishnan, S., Warke, V. G., Nambiar, M. P., Tsokos, G. C. & Farber, D. L. The FcR gamma subunit and Syk kinase replace the CD3 zeta-chain and ZAP-70 kinase in the TCR signaling complex of human effector CD4 T cells. *J. Immunol.* **170**, 4189–4195 (2003).
50. Lanier, L. L. Up on the tightrope: natural killer cell activation and inhibition. *Nat. Immunol.* **9**, 495–502 (2008).

Methods

Cell culture

HEK293F cells (Thermo) were cultured in a humidified shaker with 5% CO_2 and 55% humidity at 37 °C in FreeStyle 293 Expression Medium (Thermo). HEK293T cells (American Type Culture Collection) were cultured in DMEM (Gibco) supplemented with 1% penicillin–streptomycin (Gibco) and 10% fetal bovine serum (FBS; PAN-Biotech) in a humidified incubator at 37 °C with 5% CO_2. RBL-2H3 cells (American Type Culture Collection) were cultured in MEM (Gibco) supplemented with 1% penicillin–streptomycin and 10% FBS.

FcεRI expression and purification

For recombinant expression in HEK293F cells, genes encoding FcεRIα (human: Uniprot P12319; rat: Uniprot P12371) and FcεRIβ (Uniprot Q01362 and P13386 for human and rat FcεRIβ, respectively) were cloned into the pcDNA3.1 vector, and separated by a region encoding a 2A peptide to facilitate their co-expression. Genes encoding FcRγ (Uniprot P30273 and P20411 for human and rat FcRγ) were cloned into the pcDNA3.1 vector with a C-terminal Flag tag. HEK293F cells were grown to a density of 2×10^6 cells per millilitre and then transfected with the two plasmids encoding FcεRIα–FcεRIβ and FcRγ. For 1 l cell culture, 2 mg of the two plasmids (at a 3:1 ratio) was mixed with 4 mg of 40-kDa linear polyethylenimine (PEI; Polysciences) in 50 ml fresh medium, and incubated for 30 min before transfection. Transfected cells were cultured for another 2 days, and then the cells were collected by centrifugation and flash-frozen in liquid nitrogen.

For protein purification, thawed cell pellets were resuspended in solubilization buffer containing 20 mM HEPES pH 7.4, 150 mM NaCl, 10% (v/v) glycerol, 1% (w/v) lauryl maltose neopentyl glycol (LMNG; Anatrace), 0.1% (w/v) CHS (Anatrace) and 1 mM ethylenediaminetetraacetic acid (EDTA) supplemented with 1× protease inhibitor cocktail (Bimake). The sample was rotated for 2 h at 4 °C followed by centrifugation at 40,000 r.p.m. for 1 h using a 70 Ti fixed-angle rotor (Beckman Coulter). After the removal of insoluble debris, the supernatant was loaded onto a gravity column with anti-Flag antibody affinity resin (GenScript). The resin was washed extensively with a buffer containing 20 mM HEPES pH 7.4, 150 mM NaCl, 0.01% (w/v) LMNG and 0.001% (w/v) CHS. The FcεRI protein was then eluted in the wash buffer supplemented with 0.2 mg ml^{-1} 3× Flag peptide (NJPeptide). The eluted protein was concentrated using a 10,000-molecular-weight cutoff concentrator (Millipore) and then further purified by size-exclusion chromatography (SEC) using a Sepharose 6 column (Cytiva). The SEC buffer contained 20 mM HEPES, pH 7.4, 100 mM NaCl, 0.001% LMNG, 0.0001% CHS and 0.00033% glyco-diosgenin (Anatrace). The peak fractions were collected and concentrated using a 10,000-molecular-weight cutoff concentrator, and used fresh for the preparation of the Fcε–FcεRI complex.

For purification of the endogenous rat FcεRI from RBL-2H3 cells, approximately 2×10^9 RBL-2H3 cells were collected from one hundred 15-cm culture dishes. During solubilization of the cells in buffer containing 20 mM HEPES pH 7.4, 150 mM NaCl, 10% (v/v) glycerol, 1% (w/v) LMNG, 0.1% (w/v) CHS, 1 mM EDTA and 1× protease inhibitor cocktail, 0.5 mg rat Fcε with a C-terminal Flag tag was added for FcεRI binding and enrichment. The Fcε–FcεRI complex was then isolated using Flag affinity chromatography as described above, and the elution buffer contained 20 mM HEPES, pH 7.4, 100 mM NaCl, 0.001% LMNG, 0.0001% CHS and 0.00033% glyco-diosgenin. The eluate was concentrated and used immediately for cryo-EM sample preparation.

Fcε, anti-DNP IgE and anti-DNP IgE–sfGFP expression and purification

For expression of Fcε used in cryo-EM analysis, genes encoding human Fcε (Uniprot P01854-1, residues 106–428) and rat Fcε (Uniprot P01855, residues 97–429) were cloned into the pcDNA3.1 vector with a murine κ-signal peptide (MSVPTQVLGLLLLWLTDARC), a C-terminal 6× His tag and a Flag tag. For expression of rat anti-DNP IgE used in the degranulation assay, DNA fragments encoding the heavy-chain Fab region (GenBank AJO71810.1) of mouse anti-DNP and light chain (GenBank AJO71811.1) were synthesized with an N-terminal interleukin-2 signal peptide (GenScript). The full-length heavy chain was then generated by fusing this partial heavy chain with rat Fcε, followed by a C-terminal 6× His tag, and was installed into the pcDNA3.1 vector. The light chain was also cloned to the pcDNA3.1 vector. For expression of human anti-DNP IgE–sfGFP and rat Fcε–sfGFP used in cell surface expression analysis, the corresponding heavy chain or Fcε fragment was fused with sfGFP (GenBank QLI61463.1) and was subcloned into the pcDNA3.1 vector.

HEK293F cells at a density of 1×10^6 cells per millilitre were transiently transfected with the plasmids using PEI. For full-length IgE antibody, plasmids encoding the heavy chain and the light chain were transfected at a 1:1 ratio. After 4 days of transfection, the culture supernatant was collected by centrifugation and cell debris was removed using a 0.45 μM filter. Then the supernatant was concentrated and exchanged to buffer containing 25 mM Tris, pH 8.0, and 150 mM NaCl using a Hydrosart Ultrafilter (Sartorius). The proteins were purified first using Ni-NTA affinity chromatography, followed by a Superdex 200 column (Cytiva) equilibrated with buffer containing 20 mM HEPES, pH 7.4, and 100 mM NaCl. The monodisperse peak fractions were collected and concentrated. The concentrated protein was aliquoted, flash-frozen in liquid nitrogen and stored at −80 °C until use.

Cryo-EM sample preparation and data collection

Human Fcε and recombinant human FcεRI, as well as rat Fcε and recombinant rat FcεRI, were mixed at a 2:1 molar ratio and incubated on ice for 30 min. Then the complexes were loaded onto a Sepharose 6 column equilibrated with FcεRI SEC buffer. The monomeric peak fraction of the complex was collected and concentrated to 5 mg ml^{-1} for cryo-EM sample preparation. For the samples supplemented with fluorinated octyl maltoside (FOM; Anatrace), the complex concentration was increased to 10 mg ml^{-1}, and FOM was added to the samples fresh at a final concentration of 0.5 mM. For the complex between rat Fcε and endogenous rat FcεRI, the protein complex eluted from Flag affinity chromatography, at a concentration of 2.2 mg ml^{-1}, was subjected to cryo-EM sample preparation using the same protocol.

Cryo-grids were prepared using the Vitrobot Mark IV (FEI). Briefly, aliquots of 4 μl Fcε–FcεRI complex was deposited onto holey-carbon gold grids (Quantifoil Au 300 mesh R 1.2/1.3) glow-discharged for 60 s using a Solarus Model 950 Plasma cleaner (Gatan). Grids were blotted for 1 s with a force of −1 under 6 °C and 100% humidity. Then the grid was plunged into liquid ethane cooled by liquid nitrogen. Grids were screened under a 200 kV Talos Arctica microscope equipped with a Ceta camera (FEI). Data collections were carried out using a 300-kV Titan Krios G3 electron microscope with a K3 Summit direct detection camera, or a 300 kV Titan Krios G4 electron microscope with a Falcon 4 camera, and the EPU software (E Pluribus Unum; Thermo Scientific).

Cryo-EM data processing and model building

For human Fcε–FcεRI structure determination, a total of 5,300 videos for samples without FOM were collected, and 3,874 movies for samples with FOM were collected. The two datasets were processed using cryoSPARC[51]. The drift correction and dose-weighting were carried out using patch motion correction. The contrast transfer function parameters were estimated through patch contrast transfer function estimation. Micrographs with ice contamination were manually removed. Particles were picked first using the blob picker from 500 micrographs, and then were subjected to two-dimensional (2D) classification to generate 2D templates. Particle picking was then carried out automatically through the template picker, and junk particles were removed by several rounds of 2D classifications. Then a total of 431,968 and 512,559 particles from samples without and with FOM, respectively, were selected to generate an initial 3D model using ab

initio reconstruction, followed by heterogeneous refinement to further improve the map quality. The particles from the optimal class were subjected to non-uniform refinement, yielding a reconstruction with an overall resolution of 3.58 Å.

For the rat Fcε–FcεRI state 1 structure, a total of 5,408 videos for samples without FOM were collected, and 6,994 videos for samples with FOM were collected. The early data processing was basically the same as for the human Fcε–FcεRI datasets. In total, 5,525,999 (without FOM) and 4,888,063 (with FOM) particles were automatically extracted from the two datasets. Subsequently the extracted particles were subjected to 2D classification. Then the classes that showed obvious secondary structure features were selected and subjected to ab initio reconstruction and heterogeneous refinement. The particles in superior classes were then subjected to non-uniform refinement, resulting in a map with a resolution of 3.00 Å. To further improve the resolution, seed-facilitated 3D classification was carried out[52]. Several rounds of seed-facilitated 3D classification using good and biased references, as well as references with resolution gradients, were carried out. The resulting 698,272 particles were subjected to non-uniform refinement, yielding a map with a resolution of 2.89 Å. To improve the local resolution of the TM region, local refinement was carried out with a soft mask applied to encompass the detergent micelles, yielding a map with a resolution of 2.98 Å. The mask was created using UCSF Chimera and Relion[53,54]. All of the resolution estimations were based on a Fourier shell correlation of 0.143 cutoff and a local resolution map was calculated using cryoSPARC and displayed using UCSF Chimera.

For the rat Fcε–FcεRI state 2 and state 3 structures, a total of 5,627 videos for samples without FOM were collected, and 15,828 videos for samples with FOM were collected with a Falcon 4 direct electron detector. A total of 1,109,638 (without FOM) and 1,122,050 (with FOM) particles automatically extracted from the two datasets were subjected to ab initio reconstruction and heterogeneous refinement, resulting in two density maps of the Fcε–FcεRI complex in slightly different states. Particles in the same state were further refined using non-uniform refinement, generating two final reconstructions at resolutions of 3.04 Å and 2.96 Å, respectively. All of the resolution estimations were based on a Fourier shell correlation of 0.143 cutoff and a local resolution map was calculated using cryoSPARC and displayed using UCSF Chimera.

The models of rat Fcε, extracellular domain of FcεRIα and FcεRIβ were predicted by Alphafold[55]. FcRγ and the TM domain of FcεRIα were built de novo. Structure modelling and refinement were carried out using Coot and Phenix[56,57]. Figures were prepared using UCSF ChimeraX[58].

Immunoprecipitation

DNA fragments encoding codon-optimized human FcεRIα, FcγRIIIA (Uniprot P08637, residues 1–254) and FcαRI (Uniprot P24071, residues 1–287) were cloned into the pcDNA3.1 vector with a C-terminal Flag tag, respectively. A DNA fragment encoding WT human FcRγ was cloned into the pcDNA3.1 vector with a C-terminal MYC tag, and FcRγ(L39A/L42A) and FcRγ(L32/Y42A) mutants were generated by site-directed mutagenesis. The FcεRI, FcγRIIIA or FcαRI plasmid was co-transfected with the FcRγ plasmid into HEK293T cells using a 3:1 ratio. Transfected cells were cultured for 2 days before collection. Cells were rinsed with ice-cold PBS, and lysed in buffer containing 20 mM HEPES pH 7.4, 150 mM NaCl, 1% (w/v) LMNG, 0.1% (w/v) CHS and 1 mM EDTA supplemented with protease inhibitor cocktails for 1 h at 4 °C. The insoluble debris was removed by centrifugation at 16,000 r.p.m. for 20 min, and anti-Flag affinity beads were added to the supernatants and incubated for 2 h at 4 °C. Then the beads were washed three times using buffer containing 20 mM HEPES pH 7.4, 150 mM NaCl, 0.01% (w/v) LMNG and 0.001% (w/v) CHS. Co-immunoprecipitated protein was eluted using wash buffer supplemented with 0.2 mg ml^{-1} 3× Flag peptide. The results were analysed through immunoblotting using antibodies to Flag tag (1:1,000, GenScript), MYC tag (1:1,000, Santa Cruz Biotechnology) and goat anti-mouse IgG horseradish peroxidase (1:15,000, Jackson).

Generation of RBL-2H3 *FcRγ*-knockout cells

The RBL-2H3 *FcRγ*$^{-/-}$ cell line was generated using the CRISPR–Cas9 genome editing technique following a previously established protocol[32]. The sgRNA (5′-GCAAGAACAAGATCACCGCT-3′) targeting FcRγ was designed and cloned into the pX458 vector. A total of 10 μg plasmids was transfected into 10^6 RBL-2H3 cells using the 4D-Nucleofector System (Lonza) with the DS-150 program. Two days after electroporation, cells co-expressing sgRNA and Cas9 were sorted using a FACSAria Fusion cell sorter (BD Biosciences). After 1 week of culture, the cells were stained with rat Fcε–sfGFP, and cells without surface expression of FcεRI were sorted and enriched to generate a pool of *FcRγ*-knockout cells.

Generation of RBL-2H3 stable cell lines

Genes encoding human WT or FcRγ mutants with a C-terminal mCherry tag were cloned into the pQCXIP vector. The plasmids were co-transfected with the helper plasmid pCL10A1 using PEI. After incubation at 37 °C for 3 days, the culture medium was collected and viruses were concentrated through PEG precipitation. High-titre viruses together with 10 μg ml^{-1} Polybrene (Sigma-Aldrich) were added to RBL-2H3 cells cultured in MEM (Gibco) with 15% FBS. The cells stably expressing WT or mutant truncated FcRγ were screened through two rounds of fluorescence-activated cell sorting using a FACSAria III cell sorter (BD Biosciences). The expression levels of each stable cell line were analysed using a CytoFLEX flow cytometer.

Flow cytometry for cell surface expression analyses

For cell surface expression analysis of FcεRIα, FcγRIIIA and FcαRI on HEK293T cells, DNA fragments encoding human FcεRIα and FcγRIIIA with a C-terminal mCherry tag, and a DNA fragment encoding FcαRI with a C-terminal sfGFP tag, were cloned into the pcDNA3.1 vector, respectively. Plasmids encoding human FcεRI, FcγRIII or FcαR complexes were transiently transfected into HEK293T cells with the same transfection ratio as described in the immunoprecipitation experiment. After 24 h, HEK293T cells expressing FcεRIα, FcγRIIIA and FcαRI were stained with anti-DNP human IgE–sfGFP (prepared in-house as described above), FITC anti-human CD16 antibody (Biolegend) and PE anti-human CD89 (Biolegend), respectively. After incubation at 4 °C for 30 min, the cells were washed twice with PBS. Then the cells were resuspended in DMEM supplemented with 2% FBS. For cell surface expression analysis of FcεRIα on RBL-2H3 cells, cells were stained with rat Fcε–sfGFP at 4 °C for 30 min. Then the cells were resuspended in MEM supplemented with 2% FBS.

The surface expression level was analysed using a CytoFLEX flow cytometer (Beckman). Gating strategies for the flow cytometry experiments are presented in Extended Data Fig. 7. Flow cytometry data were analysed using FlowJo software. For analysis in HEK293T cells, the proportion of cell surface expression was normalized by the ratio of the number of surface-staining-positive cells to the total number of cells expressing corresponding Fc receptors. For analysis in RBL-2H3 cells, cell surface expression was normalized by the ratio of GFP fluorescence intensity of the cells to that of cells recovered with WT FcRγ.

Degranulation assay

The degranulation response of RBL-2H3 cells was assessed using their level of β-hexosaminidase release as previously described, with slight modifications[59]. Briefly, 1.5×10^5 RBL-2H3 cells maintained in MEM medium with 15% FBS were seeded into 12-well tissue culture plates and incubated at 37 °C overnight. Then the cells were sensitized by 2 μg rat anti-DNP IgE for 1 h at 37 °C. After washing with PBS twice, each well of cells was exchanged into Tyrode's buffer supplemented with 0.1% BSA and stimulated by adding 2 μg DNP–BSA (LGC Biosearch Technologies). After incubation of the sample at 37 °C for 1 h, the supernatant was collected for quantifying the released β-hexosaminidase level and the cell pellets were lysed with an equal volume of 1% (w/w) Triton

X-100 Tyrode's buffer for measuring the remaining β-hexosaminidase level. A 40 µl volume of supernatant and cell lysate was incubated with 40 µl 1 mM *p*-nitrophenyl *N*-acetyl-α-D-glucosaminide (Sigma-Aldrich) in 100 mM citrate buffer (pH 4.5) for 1 h at 37 °C. The reactions were terminated by adding 200 µl 200 mM glycine (pH 10.7). The absorbance of each well was measured immediately by a Cytation 5 microplate luminometer (BioTek). The percentage of β-hexosaminidase release was calculated according to the following formula: percentage of β-hexosaminidase release = $\text{absorbance}_{\text{supernatant}}/(\text{absorbance}_{\text{supernatant}} + \text{absorbance}_{\text{lysate}}) \times 100\%$.

Reporting summary

Further information on research design is available in the Nature Portfolio Reporting Summary linked to this article.

Data availability

Cryo-EM density maps have been deposited in the Electron Microscopy Data Bank with the accession codes EMD-39033 (human Fcε–FcεRI complex), EMD-39029 (rat Fcε–FcεRI complex, state 1), EMD-39032 (rat Fcε–FcεRI complex TM region, state 1), EMD-60089 (rat Fcε–FcεRI complex, state 2) and EMD-60090 (rat Fcε–FcεRI complex, state 3). Structural coordinates have been deposited in the PDB with the accession codes 8Z0T, 8Y81, 8Y84, 8ZGS and 8ZGT. The other structural coordinates used in this study are available from PDB (2Y7Q, 6VJA, 7FJD and 8JC0). Source data are provided with this paper.

51. Punjani, A., Rubinstein, J. L., Fleet, D. J. & Brubaker, M. A. cryoSPARC: algorithms for rapid unsupervised cryo-EM structure determination. *Nat. Methods* **14**, 290–296 (2017).
52. Wang, N. et al. Structural basis of human monocarboxylate transporter 1 inhibition by anti-cancer drug candidates. *Cell* **184**, 370–383 (2021).
53. Pettersen, E. F. et al. UCSF Chimera-a visualization system for exploratory research and analysis. *J. Comput. Chem.* **25**, 1605–1612 (2004).
54. Zivanov, J. et al. New tools for automated high-resolution cryo-EM structure determination in RELION-3. *eLife* **7**, e42166 (2018).
55. Jumper, J. et al. Highly accurate protein structure prediction with AlphaFold. *Nature* **596**, 583–589 (2021).
56. Emsley, P., Lohkamp, B., Scott, W. G. & Cowtan, K. Features and development of Coot. *Acta Crystallogr. D* **66**, 486–501 (2010).
57. Adams, P. D. et al. PHENIX: a comprehensive Python-based system for macromolecular structure solution. *Acta Crystallogr. D* **66**, 213–221 (2010).
58. Pettersen, E. F. et al. UCSF ChimeraX: structure visualization for researchers, educators, and developers. *Protein Sci.* **30**, 70–82 (2021).
59. Bawazir, M., Amponnawarat, A., Hui, Y., Oskeritzian, C. A. & Ali, H. Inhibition of MRGPRX2 but not FcεRI or MrgprB2-mediated mast cell degranulation by a small molecule inverse receptor agonist. *Front. Immunol.* **13**, 1033794 (2022).

Acknowledgements We thank the cryo-EM and the high-performance computing platforms of Peking University and Changping Laboratory for support with data collection and computation, and the National Center for Protein Sciences at Peking University for assistance with the flow cytometry facilities, the BioTek plate reader and the 4D-Nucleofector system. This work received support from the National Natural Science Foundation of China (32325018) and the Qidong-SLS Innovation Fund to J.X., as well as from Changping Laboratory.

Author contributions M.D. and S.D. made equal contributions to this work. J.X. conceived and supervised the project. M.D. and S.D. conducted the structural studies. M.D. and S.D. carried out the functional experiments with assistance from H.H. M.D. and S.D. wrote the first draft of the manuscript, and J.X. revised and finalized it.

Competing interests The authors declare no competing interests.

Additional information

Supplementary information The online version contains supplementary material available at https://doi.org/10.1038/s41586-024-07864-5.

Correspondence and requests for materials should be addressed to Shuo Du or Junyu Xiao.

Peer review information *Nature* thanks Sonya Kumar Bharathkar, Falk Nimmerjahn and the other, anonymous, reviewer(s) for their contribution to the peer review of this work. Peer reviewer reports are available.

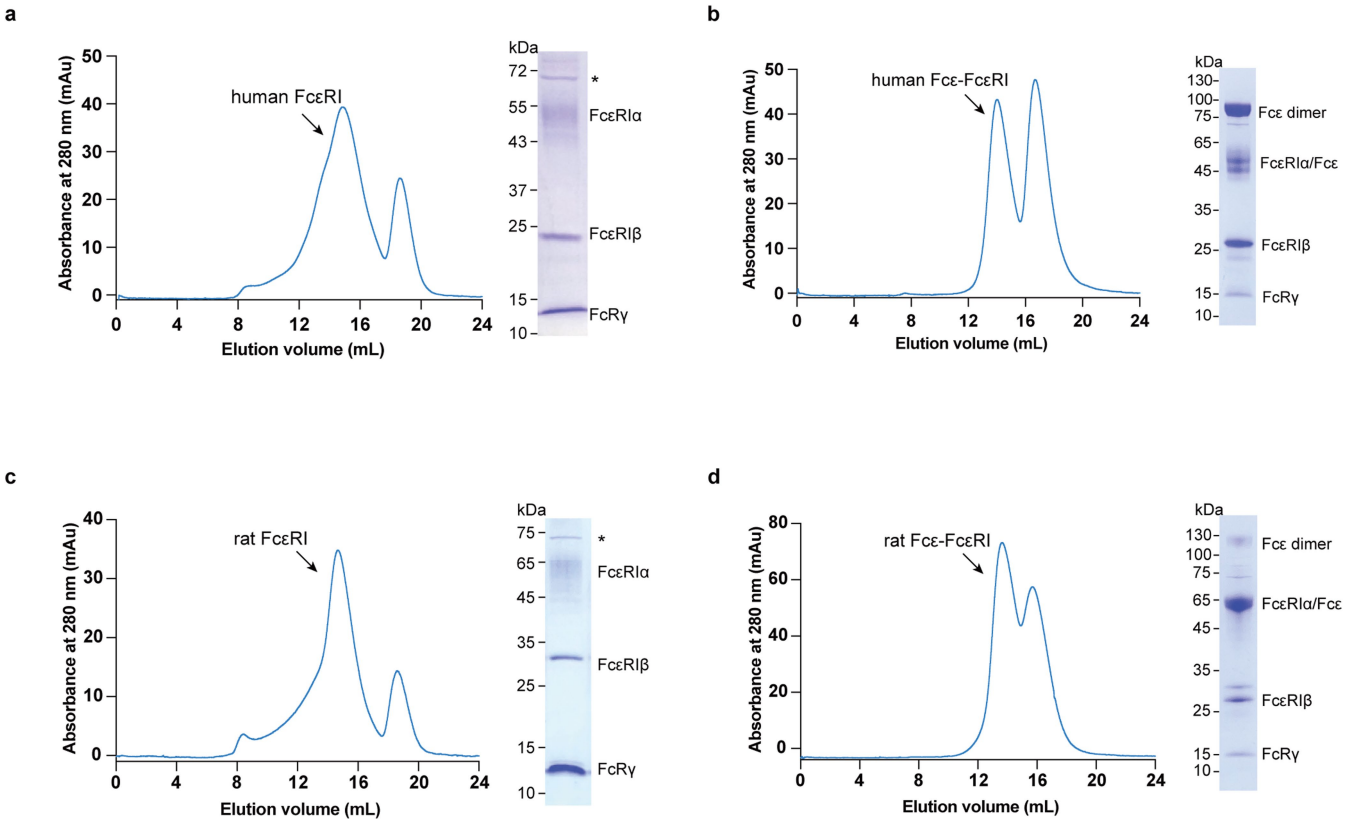

Extended Data Fig. 1 | Purification of Fcε and the Fcε–FcεRI complex. a. Size-exclusion chromatography and SDS-PAGE analysis of human FcεRI. The complex was visualized on a reducing SDS-PAGE through Coomassie blue staining. The asterisk indicates an unspecific protein from the HEK293F cells. These results, along with the subsequent protein purification experiments, have been replicated in at least two independent experiments. b. Size-exclusion chromatography and SDS-PAGE analysis of human Fcε–FcεRI complex. c. Size-exclusion chromatography and SDS-PAGE analysis of rat FcεRI. d. Size-exclusion chromatography and SDS-PAGE analysis of rat Fcε–FcεRI complex.

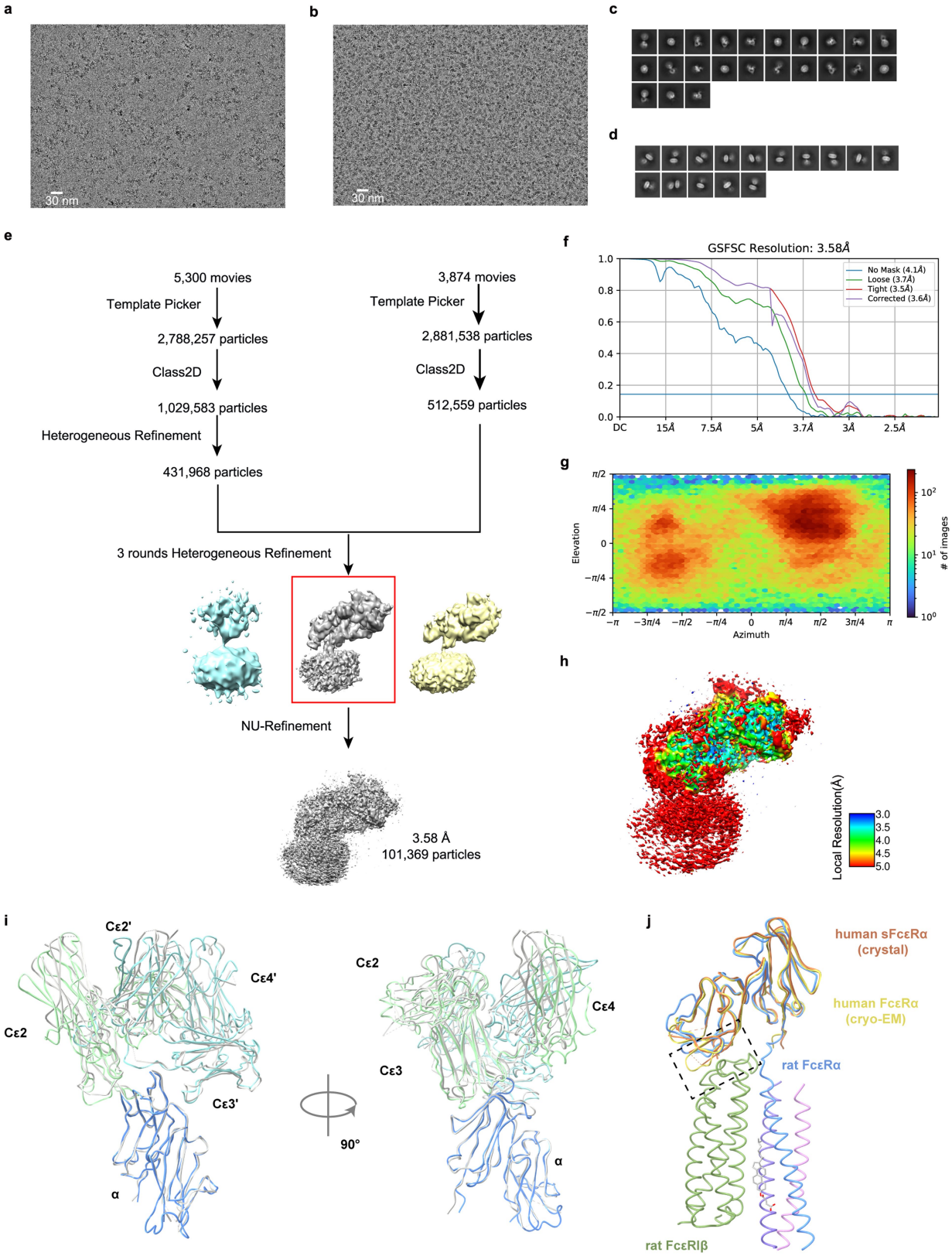

Extended Data Fig. 2 | See next page for caption.

Extended Data Fig. 2 | Cryo-EM analysis of human Fcε–FcεRI complex. a. A representative cryo-EM micrograph of human Fcε–FcεRI sample without fluorinated octyl maltoside (FOM). The micrograph shown is an example image from a full dataset consisting of 5,300 micrographs. b. A representative cryo-EM micrograph of the human Fcε–FcεRI sample with FOM. The micrograph shown is an example image from a full dataset consisting of 3,874 micrographs. c. 2D class averages of human Fcε–FcεRI sample without FOM. d. 2D class averages of human Fcε–FcεRI sample with FOM. e. Flowchart of the cryo-EM analysis for human Fcε–FcεRI complex. f. Gold-standard Fourier shell correlation (GSFSC) curve of the final density map. The reconstruction evaluated by the 0.143 FSC value (blue line) shows an average resolution of 3.58 Å. g. Angular particle distribution of the particles in the final round of 3D refinement. h. Local resolution estimation of the density map. i. Structural comparison between the human Fcε–FcεRI cryo-EM structure (this study) and the Fcε–sFcεRIα crystal structure (PDB ID: 2Y7Q). The two chains of Fcε and FcεRIα in the cryo-EM structure are depicted in cyan, green, and blue, respectively, while the Fcε–sFcεRIα crystal structure is displayed in white. j. Structural comparison among the human Fcε–FcεRI cryo-EM structure (this study), the human Fcε–sFcεRIα crystal structure (PDB ID: 2Y7Q), and the rat Fcε–FcεRI cryo-EM structure (this study). The dashed box highlights subtle structural differences in the FcεRIα region that is involved in interacting with FcεRIβ in these structures.

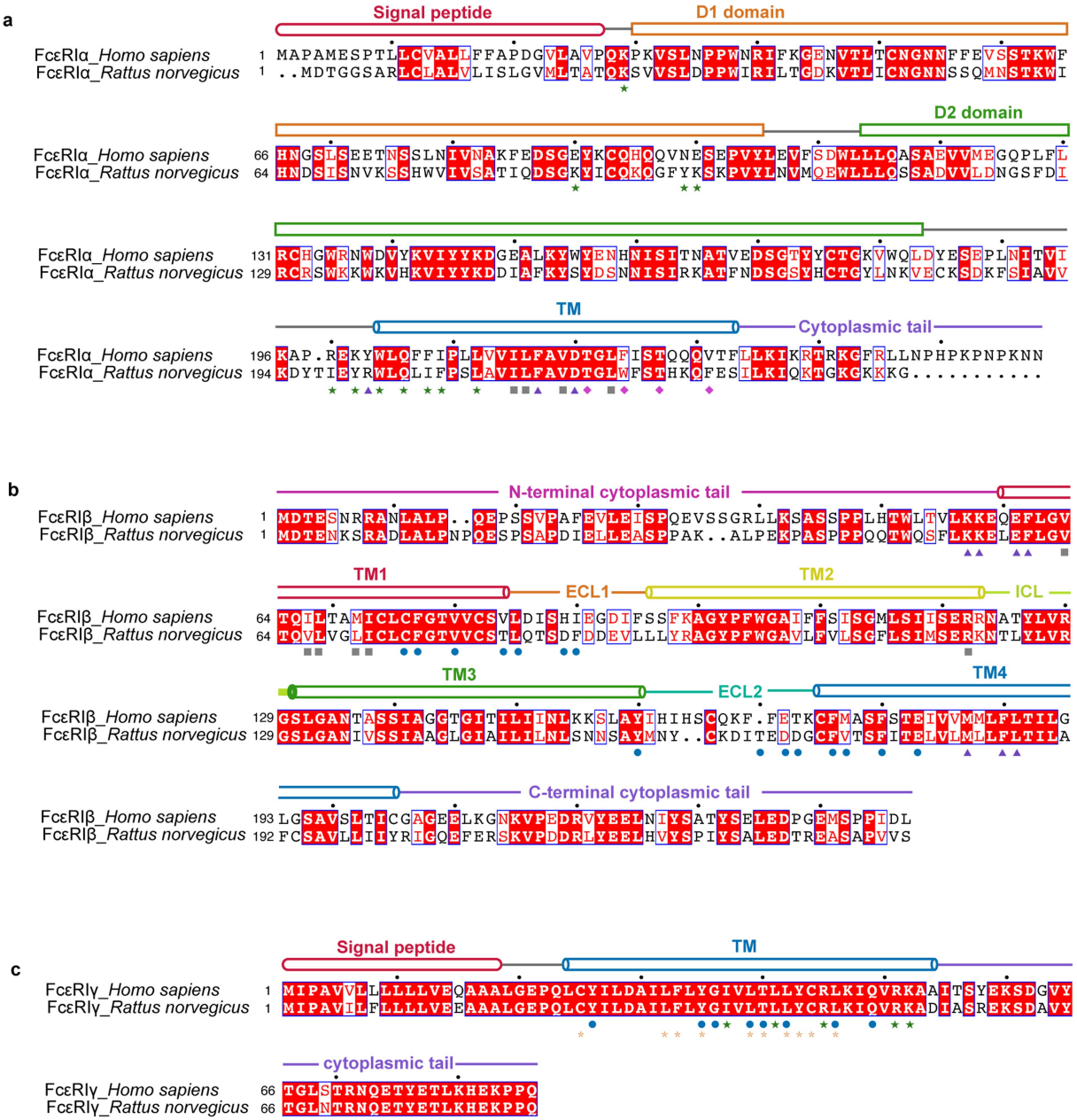

Extended Data Fig. 3 | Sequence alignments of human and rat FcεRI subunits. a. Sequence alignments of FcεRIα. Residues involved in interactions with FcεRIβ, FcRγ, FcRγ′, and CHS are indicated with green stars, purple triangles, pink diamonds, and grey squares, respectively. b. Sequence alignments of FcεRIβ. Residues involved in interactions with FcεRIα, FcRγ, and CHS are indicated with blue circles, purple triangles, and grey squares, respectively. c. Sequence alignments of FcRγ. Residues involved in dimerization, interactions with FcεRIα, and interactions with FcεRIβ are indicated with orange asterisks, blue circles, and green stars, respectively.

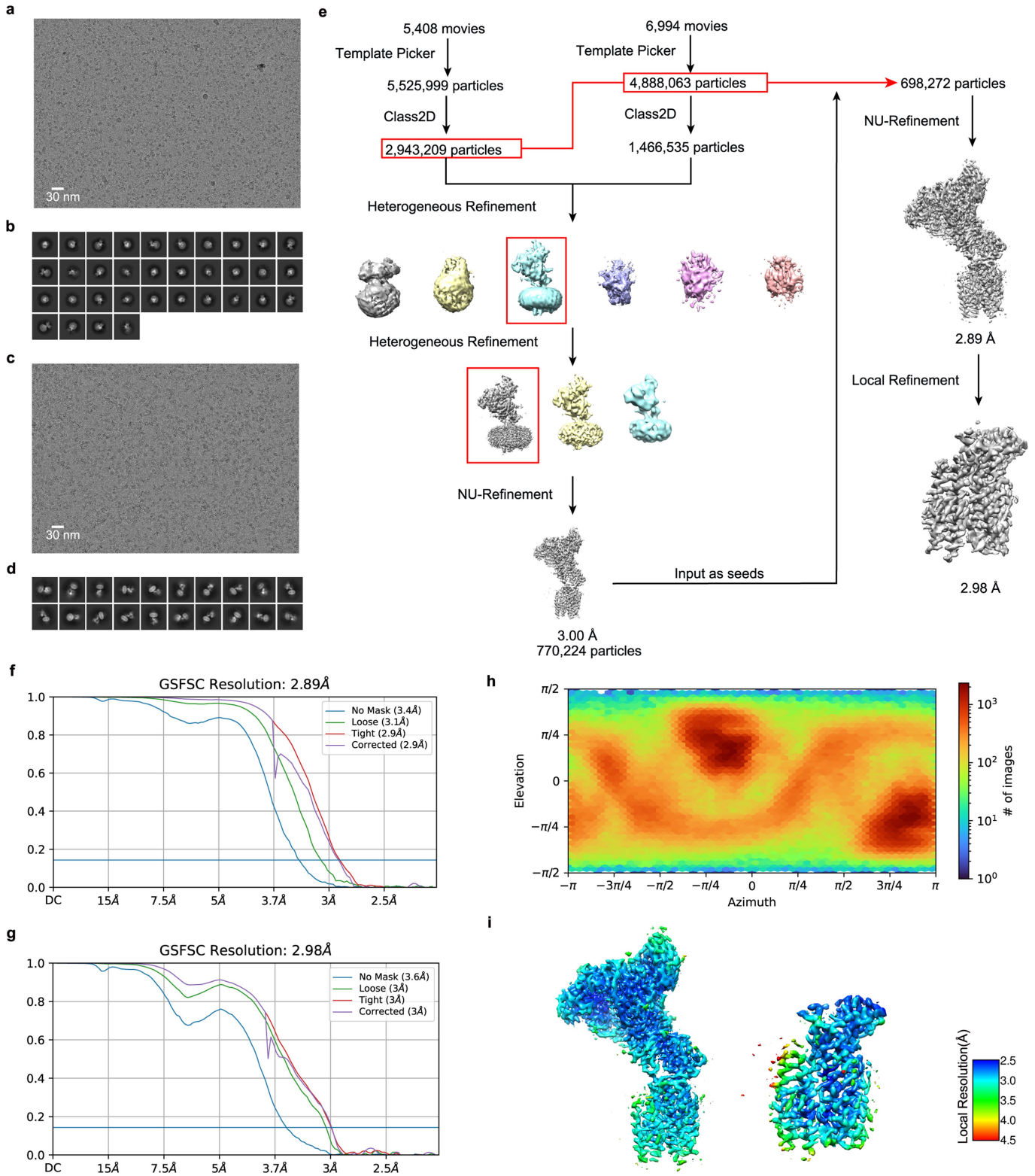

Extended Data Fig. 4 | Cryo-EM analysis of rat Fcε–FcεRI complex (state1). a. A representative raw cryo-EM micrograph of the rat Fcε–FcεRI sample without FOM. The micrograph shown is an example image from a full dataset consisting of 5,408 micrographs. b. 2D class averages of the rat Fcε–FcεRI sample without FOM. c. A representative raw cryo-EM micrograph of the rat Fcε–FcεRI sample with FOM. The micrograph shown is an example image from a full dataset consisting of 6,994 micrographs. d. 2D class averages of the rat Fcε–FcεRI sample with FOM. e. Flowchart of the cryo-EM analysis for the rat Fcε–FcεRI complex. f. Gold-standard Fourier shell correlation (GSFSC) curve of the final density map. The reconstruction evaluated by the 0.143 FSC value (blue line) shows an average resolution of 2.89 Å. g. Gold-standard Fourier shell correlation (GSFSC) curve of the local density map. The reconstruction evaluated by the 0.143 FSC value (blue line) shows an average resolution of 2.98 Å. h. Angular particle distribution of the particles in the final round of 3D refinement. i. Local resolution estimation of the global density map (left panel) and local density map (right panel).

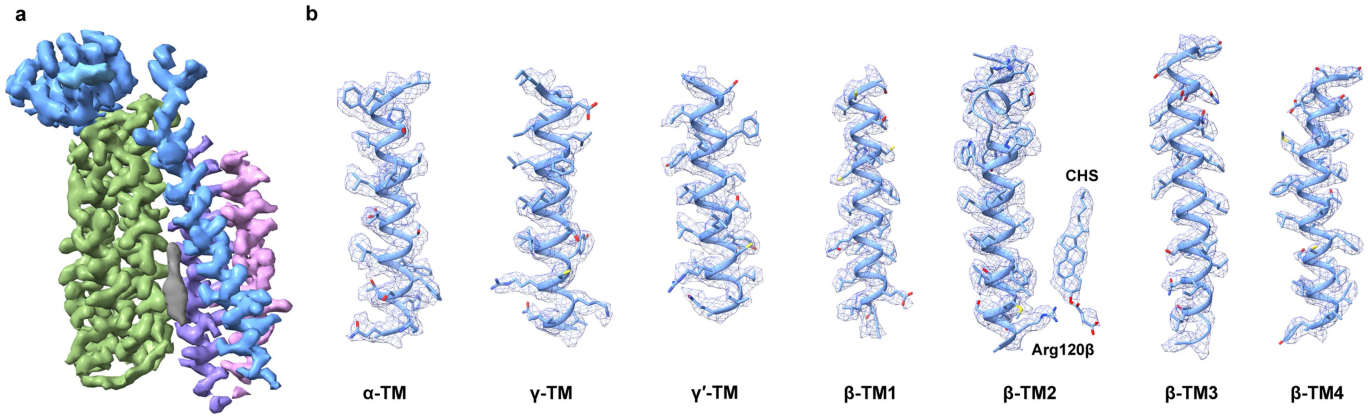

Extended Data Fig. 5 | Local density map of the TM regions. a. Local density map of FcεRI TM region. Density maps for TM helices of FcεRIα, FcεRIβ, and the two chains of FcRγ are shown in blue, green, purple, and magenta, respectively. The density map of CHS molecular is colored grey. b. The representative EM maps for TM region in FcεRI complex. The maps are displayed as blue meshes with a similar threshold.

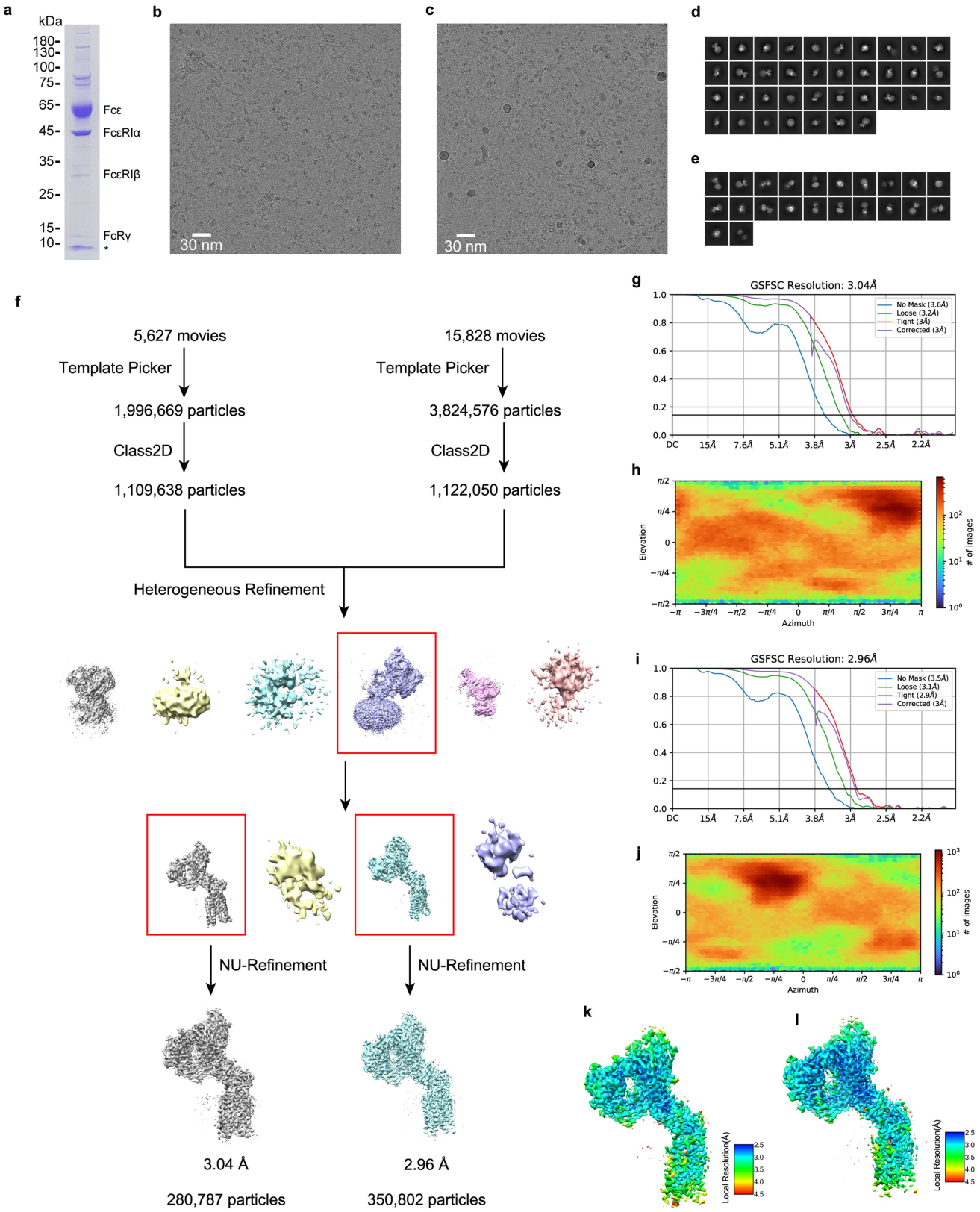

Extended Data Fig. 6 | See next page for caption.

Extended Data Fig. 6 | Cryo-EM structures of the rat Fcε–FcεRI structures determined using the endogenous FcεRI complex isolated from the RBL-2H3 cells. a. Purification of the rat Fcε–FcεRI complex, visualized on a reducing SDS-PAGE by Coomassie staining. The asterisk indicates the 3× Flag peptides. b. A representative raw cryo-EM micrograph of the rat Fcε–FcεRI sample without FOM. The micrograph shown is an example image from a full dataset consisting of 5,627 micrographs. c. A representative raw cryo-EM micrograph of the rat Fcε–FcεRI sample with FOM. The micrograph shown is an example image from a full dataset consisting of 15,828 micrographs. d. 2D class averages of the rat Fcε–FcεRI sample without FOM. e. 2D class averages of the rat Fcε–FcεRI sample with FOM. f. Flowchart of the cryo-EM analyses. g. Gold-standard Fourier shell correlation (GSFSC) curve of the final density map for the state2 structure. The reconstruction evaluated by the 0.143 FSC value (blue line) shows an average resolution of 3.04 Å. h. Angular particle distribution of the particles for the reconstruction of the state2 structure in the final round of 3D refinement. i. Gold-standard Fourier shell correlation (GSFSC) curve of the final density map for the state3 structure. The reconstruction evaluated by the 0.143 FSC value (blue line) shows an average resolution of 2.96 Å. j. Angular particle distribution of the particles for the reconstruction of the state3 structure in the final round of 3D refinement. k. Local resolution estimation of the density map for the state2 structure. l. Local resolution estimation of the density map for the state3 structure.

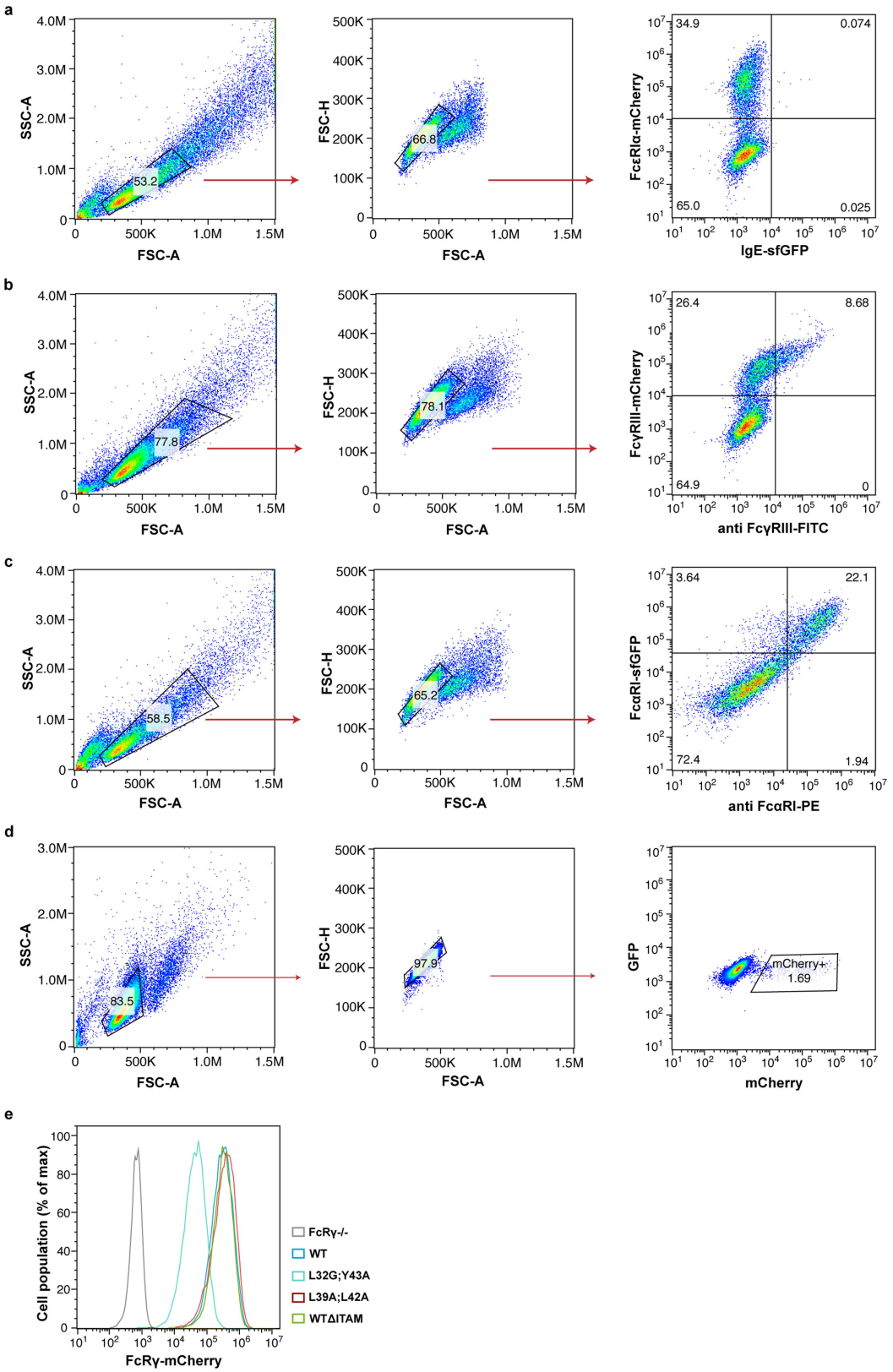

Extended Data Fig. 7 | Flow cytometry experiments. a. Gating strategy used for analyzing the cell surface FcεRIα levels. The strategy used for cells expressing only the FcεRIα subunit is shown here as an example. b. Gating strategy used for analyzing the cell surface FcγRI levels. The strategy used for cells expressing only the FcγRI subunit is shown as an example. c. Gating strategy used for analyzing the cell surface FcαRI levels. The strategy used for cells expressing only the FcαRI subunit is shown as an example. d. Gating strategy used for sorting of the *FcRγ*−/− cells that stably expressing WT or mutant FcRγ. e. Flow cytometry analyses of the expression levels of WT, L39A;L42A, L32G;L43A and $WT_{\Delta ITAM}$ in RBL-2H3 *FcRγ*−/− cells.

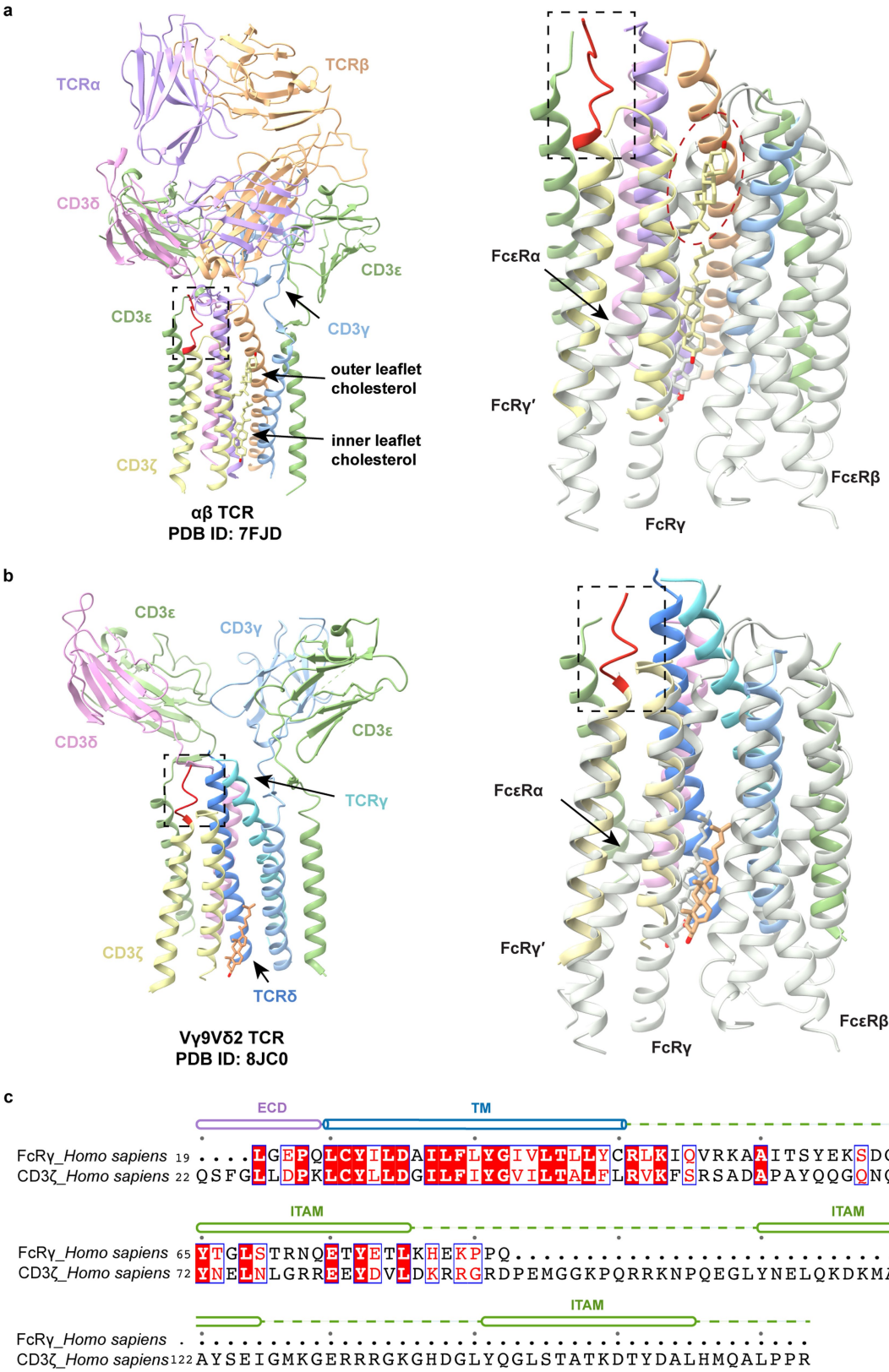

Extended Data Fig. 8 | Structural comparisons of the FcεRI and TCR–CD3 complexes. a. The structure of αβ TCR–CD3 complex with two bound cholesterols (PDB ID: 7FJD). TCRα, TCRβ, CD3γ, CD3ε, CD3δ, and CD3ζ are depicted in purple, orange, blue, green, pink, and yellow, respectively. The extracellular region of one CD3ζ that interacts with the membrane-proximal regions of TCRα and CD3δ is depicted in red and highlighted in a dashed box. The two cholesterol molecules are illustrated in stick representation. In the right panel, the TM region of rat FcεRI complex, depicted in white, is superimposed onto the TM regions of the αβ TCR–CD3 complex, by aligning the FcRγ dimer with the CD3ζ dimer. Only one cholesterol-like molecule, located at a position corresponding to the inner leaflet of the membrane, was observed in the FcεRI structure. The tilted FcεRIα's TM would obstruct the binding of the outer-leaflet cholesterol, as indicated using a red dashed oval. b. The structure of the cholesterol-bound Vγ9Vδ2 γδ TCR–CD3 complex (PDB ID: 8JC0) and its comparison with the rat FcεRI. c. Sequence alignments of human FcRγ and CD3ζ.

Extended Data Table 1 | Cryo-EM data collection, refinement and validation statistics

	Rat Fcε–FcεRI state1 (EMDB 39029) (PDB 8Y81)	Rat Fcε–FcεRI state1 TM (EMDB 39032) (PDB 8Y84)	Human Fcε–FcεRI (EMDB 39033) (PDB 8Z0T)	Rat Fcε–FcεRI state2 (EMDB 60089) (PDB 8ZGS)	Rat Fcε–FcεRI state3 (EMDB 60090) (PDB 8ZGT)
Data collection and processing					
Magnification	81,000	81,000	81,000	130,000	130,000
Voltage (kV)	300	300	300	300	300
Electron exposure (e^{-}/Å^2)	60	60	60	60	60
Defocus range (μm)	–1.0 to –1.5	–1.0 to –1.5	–1.0 to –1.5	–1.0 to –1.5	–1.0 to –1.5
Pixel size (Å)	1.07	1.07	1.07	0.95	0.95
Symmetry imposed	C1	C1	C1	C1	C1
Initial particle images (no.)	10,414,062	10,414,062	5,669,795	5,821,245	5,821,245
Final particle images (no.)	698,272	698,272	101,369	280,787	350,802
Map resolution (Å) (FSC threshold 0.143)	2.89	2.98	3.58	3.04	2.96
Map resolution range (Å)	250–2.89	250–2.98	250–3.58	250–3.04	250–2.96
Refinement					
Initial model used	Alphafold2	Alphafold2	2Y7Q	Alphafold2	Alphafold2
Model resolution range (Å)	250–2.89	250–2.98	250–3.58	250–3.04	250–2.96
Map sharpening *B* factor (Å^2)	–117.6	–89.3	–110.0	–99.7	–102.1
Model composition					
Non–hydrogen atoms	8,916	2,169	6,556	8,916	8,916
Protein residues	1,077	268	802	1,077	1,077
Ligands	14	1	17	14	14
B factors (Å^2)					
Protein	40.01	58.34	84.94	64.86	52.12
Ligand	36.48	56.75	75.59	66.60	56.17
R.m.s. deviations					
Bond lengths (Å)	0.006	0.006	0.005	0.006	0.004
Bond angles (°)	0.959	1.197	0.930	0.606	0.763
Validation					
MolProbity score	1.56	1.26	1.76	1.60	1.82
Clashscore	5.39	4.95	6.21	5.55	2.24
Poor rotamers (%)	0.10	0.00	0.98	0.40	4.14
Ramachandran plot					
Favored (%)	96.06	98.46	93.59	95.67	95.02
Allowed (%)	3.85	1.54	6.41	4.33	4.88
Disallowed (%)	0.09	0.00	0.00	0.00	0.09

Cryo-EM density maps and structural coordinates have been deposited in the Electron Microscopy Data Bank (EMDB) and Protein Data Bank (PDB), respectively, under the corresponding accession codes shown in the table.

nature portfolio

Corresponding author(s): Junyu Xiao

Last updated by author(s): Jul 1, 2024

Reporting Summary

Nature Portfolio wishes to improve the reproducibility of the work that we publish. This form provides structure for consistency and transparency in reporting. For further information on Nature Portfolio policies, see our Editorial Policies and the Editorial Policy Checklist.

Statistics

For all statistical analyses, confirm that the following items are present in the figure legend, table legend, main text, or Methods section.

n/a	Confirmed
☐	☒ The exact sample size (*n*) for each experimental group/condition, given as a discrete number and unit of measurement
☐	☒ A statement on whether measurements were taken from distinct samples or whether the same sample was measured repeatedly
☐	☒ The statistical test(s) used AND whether they are one- or two-sided *Only common tests should be described solely by name; describe more complex techniques in the Methods section.*
☒	☐ A description of all covariates tested
☒	☐ A description of any assumptions or corrections, such as tests of normality and adjustment for multiple comparisons
☐	☒ A full description of the statistical parameters including central tendency (e.g. means) or other basic estimates (e.g. regression coefficient) AND variation (e.g. standard deviation) or associated estimates of uncertainty (e.g. confidence intervals)
☐	☒ For null hypothesis testing, the test statistic (e.g. *F*, *t*, *r*) with confidence intervals, effect sizes, degrees of freedom and *P* value noted *Give P values as exact values whenever suitable.*
☒	☐ For Bayesian analysis, information on the choice of priors and Markov chain Monte Carlo settings
☒	☐ For hierarchical and complex designs, identification of the appropriate level for tests and full reporting of outcomes
☒	☐ Estimates of effect sizes (e.g. Cohen's *d*, Pearson's *r*), indicating how they were calculated

Our web collection on statistics for biologists contains articles on many of the points above.

Software and code

Policy information about availability of computer code

Data collection	EPU software v2.12.1 (E Pluribus Unum, Thermo Scientific) were used to collect the cryo-EM data.
Data analysis	cryoSPARC v4.4.1 was used to process the cryo-EM data. The local resolution map was analyzed using cryoSPARC's built-in local resolution estimation tool and displayed using UCSF ChimeraX v1.5. Structural modeling and refinement were performed using Coot v0.9.8.1 and Phenix v1.20 and v1.21. FlowJo software v10.8.1 and GraphPad Prism v9.5.1 were used to analyze flow cytometry data.

For manuscripts utilizing custom algorithms or software that are central to the research but not yet described in published literature, software must be made available to editors and reviewers. We strongly encourage code deposition in a community repository (e.g. GitHub). See the Nature Portfolio guidelines for submitting code & software for further information.

Data

Policy information about availability of data

All manuscripts must include a data availability statement. This statement should provide the following information, where applicable:

- Accession codes, unique identifiers, or web links for publicly available datasets
- A description of any restrictions on data availability
- For clinical datasets or third party data, please ensure that the statement adheres to our policy

Cryo-EM density maps have been deposited in the Electron Microscopy Data Bank with accession codes EMD-39033 (human Fcε-FcεRI complex), EMD-39029 (rat

Fcε-FcεRI complex, state1), EMD-39032 (rat Fcε-FcεRI complex TM region, state1), EMD-60089 (rat Fcε-FcεRI complex, state2) and EMD-60090 (rat Fcε-FcεRI complex, state3). Structural coordinates have been deposited in the Protein Data Bank (PDB) with the accession codes 8Z0T, 8Y81, 8Y84, 8ZGS and 8ZGT.
To prepare figures, we used structural information from the PDB with the accession codes 2Y7Q, 6VJA, 7FJD and 8JC0.
All data are available in the manuscript and the Supplementary Information.

Research involving human participants, their data, or biological material

Policy information about studies with human participants or human data. See also policy information about sex, gender (identity/presentation), and sexual orientation and race, ethnicity and racism.

Reporting on sex and gender	N/A
Reporting on race, ethnicity, or other socially relevant groupings	N/A
Population characteristics	N/A
Recruitment	N/A
Ethics oversight	N/A

Note that full information on the approval of the study protocol must also be provided in the manuscript.

Field-specific reporting

Please select the one below that is the best fit for your research. If you are not sure, read the appropriate sections before making your selection.

☒ Life sciences ☐ Behavioural & social sciences ☐ Ecological, evolutionary & environmental sciences

For a reference copy of the document with all sections, see nature.com/documents/nr-reporting-summary-flat.pdf

Life sciences study design

All studies must disclose on these points even when the disclosure is negative.

Sample size	The sample sizes for the cryo-EM datasets were selected to ensure the acquisition of high-resolution structures after initial examination of the cryo-EM sample. The number of particles used for cryo-EM reconstructions has been indicated in the Extended Data Fig. 2, 4, and 6.
Data exclusions	Cryo-EM particle exclusion has been performed following standard procedures in the cryoSPARC software to remove low-quality particles, and the remaining particle number has been stated in the methods section. No other data was excluded.
Replication	The functional experiments were repeated at least twice and the results were successfully reproduced. The biological independent replicate numbers were described in the respective figure legends.
Randomization	For the cryo-EM studies, the particles were randomly divided into two separate groups during the 3D refinement process, and two independent reconstructions were generated. The Fourier Shell Correlation (FSC) between the independent reconstructions is computed, and an FSC value of 0.143 (gold-standard) was used to estimate the resolution.
Blinding	Not applicable since there are no groups to allocate in this study.

Reporting for specific materials, systems and methods

We require information from authors about some types of materials, experimental systems and methods used in many studies. Here, indicate whether each material, system or method listed is relevant to your study. If you are not sure if a list item applies to your research, read the appropriate section before selecting a response.

Materials & experimental systems

n/a	Involved in the study
☐	☒ Antibodies
☐	☒ Eukaryotic cell lines
☒	☐ Palaeontology and archaeology
☒	☐ Animals and other organisms
☒	☐ Clinical data
☒	☐ Dual use research of concern
☒	☐ Plants

Methods

n/a	Involved in the study
☒	☐ ChIP-seq
☐	☒ Flow cytometry
☒	☐ MRI-based neuroimaging

Antibodies

Antibodies used

Mouse anti flag-tag antibody (GenScript, catalog no. A00187, dilution: 1:1,000), Myc antibody (Santa Cruz Biotechnology, catalog no. sc-40, dilution: 1:1,000), goat anti-mouse IgG horseradish peroxidase (Jackson, catalog no.115-035-062, dilution: 1:15,000), FITC antihuman CD16 antibody (biolegend, catalog no. 302006, dilution: 5 µL per million cells in 100 µL staining volume), PE anti-human CD89 (biolegend, catalog no. 354104, dilution: 5 µL per million cells in 100 µL staining volume).
The anti-DNP IgE antibody was prepared as described in the Methods.

Validation

The antibodies were validated by the manufacture, and the following validation statements can be found on the manufacture's website:
- The Mouse anti flag-tag antibody (clone: 5A8E5) is a high-affinity monoclonal antibody that can be used to detect DYKDDDDK-tagged proteins and recognizes DYKDDDDK tags localized at the C-terminal, N-terminal and internal region of DYKDDDDK tagged fusion proteins. The tag does not appear to interfere with the bioactivity or bio-distribution of the tagged recombinant proteins. s. Species Cross-Reactivity: N/A. Applications include ELISA, WB, IP.
- The Myc tag antibody (clone:9E10) recognizes c-Myc p67 and c-Myc tagged fusion proteins of mouse, rat, human, monkey, feline and canine origins. Species Cross-Reactivity: N/A. Applications includes WB, IP, IF, flow cytometry.
- Goat Anti-mouse IgG HRP recognizes mouse IgG (H+L). Species Cross-Reactivity: N/A. Applications: WB, ELISA.
- FITC anti-human CD16 antibody (clone: 3G8) recognizes human CD16.The antibody is quality control tested by immunofluorescent staining with flow cytometric analysis.
- PE anti-human CD89 (clone: A59) recognizes human CD89. The antibody is quality control tested by immunofluorescent staining with flow cytometric analysis.
The anti-DNP IgE antibody was validated by its ability to induce degranulation, as described in Ref. 34.

Eukaryotic cell lines

Policy information about cell lines and Sex and Gender in Research

Cell line source(s)

HEK293F (catlog no. R79007) cells were purchased from Thermo.
HEK293T (CRL-3216), and RBL-2H3 (CRL-2256) cells were originally purchased from ATCC.

Authentication

The cell lines were not authenticated.

Mycoplasma contamination

The cells were regularly tested for free of Mycoplasma contamination by standard PCR method.

Commonly misidentified lines
(See ICLAC register)

No commonly misidentified lines were used.

Plants

Seed stocks

Report on the source of all seed stocks or other plant material used. If applicable, state the seed stock centre and catalogue number. If plant specimens were collected from the field, describe the collection location, date and sampling procedures.

Novel plant genotypes

Describe the methods by which all novel plant genotypes were produced. This includes those generated by transgenic approaches, gene editing, chemical/radiation-based mutagenesis and hybridization. For transgenic lines, describe the transformation method, the number of independent lines analyzed and the generation upon which experiments were performed. For gene-edited lines, describe the editor used, the endogenous sequence targeted for editing, the targeting guide RNA sequence (if applicable) and how the editor was applied.

Authentication

Describe any authentication procedures for each seed stock used or novel genotype generated. Describe any experiments used to assess the effect of a mutation and, where applicable, how potential secondary effects (e.g. second site T-DNA insertions, mosiacism, off-target gene editing) were examined.

Flow Cytometry

Plots

Confirm that:

☒ The axis labels state the marker and fluorochrome used (e.g. CD4-FITC).

☒ The axis scales are clearly visible. Include numbers along axes only for bottom left plot of group (a 'group' is an analysis of identical markers).

☒ All plots are contour plots with outliers or pseudocolor plots.

☒ A numerical value for number of cells or percentage (with statistics) is provided.

Methodology

Sample preparation	HEK293T cells expressing FcεRIα, and FcγRIIIA and FcαRI were stained with anti-DNP IgE-sfGFP (prepared in-house as described above), FITC anti-human CD16 antibody (biolegend), and PE anti-human CD89 (biolegend), respectively. After incubation at 4°C for 30 minutes, the cells were washed twice with PBS. Then the cells were resuspended in DMEM (Gibco) supplemented with 2% FBS (PAN-Biotech).
Instrument	The surface expression level was analyzed using CytoFLEX Flow Cytometer (Beckman).
Software	Flow cytometry data were analyzed using FlowJo software (FlowJo LLC, version 10.8.1)
Cell population abundance	To generate the RBL-2H3 stable cell line, cell population were gated for mCherry-positive cells in the first round FACS, and then gated for top 10% mCherry-expression cells in the second round FACS. For cell surface expression analysis, at least 10,000 cellular events were collected for each sample.cell population were gated as described in the Extended data Fig. 7 and indicated in Figs. 4b, 5e-f.
Gating strategy	Cells were firstly gated using FSC-A/SSC-A, followed by FSC-A/FSC-H for single cells. The boundary between positive and negative is defined according to the negative controls.

☒ Tick this box to confirm that a figure exemplifying the gating strategy is provided in the Supplementary Information.